Norges miljø- og
biovitenskapelige
universitet

Master's Thesis 2017 30 ECTS
Faculty of Science and Technology
Supervisor: Professor Tor Anders Nygaard

Numerical analysis of rotor-stator interaction in a Francis turbine guide vane

Eivind Myrvold
Mechanics and Process Technology
Faculty of Science and Technology

Acknowledgements

The work presented in this thesis has been performed at the Faculty of Science and Technology at the Norwegian University of Life Sciences (NMBU) and at Rainpower Norway's offices during the autumn semester 2017.

I would like to thank Rainpower for introducing me to the topic of rotor-stator interactions, giving me access to their models and geometries, and for their financial support by covering the fee for the ANSYS license required to perform the numerical analyses. Thanks to all the employees who have assisted me during my project. In particular I am deeply grateful to my supervisor at Rainpower, turbine designer and PhD-student Petter Østby, for showing great interest in my work, for valuable discussions and for his assistance with the numerical models. His door has always been open to me and working with Petter has been a great motivation throughout the project.

I would also like to thank my supervisor at NMBU, Professor Tor Anders Nygaard, for feedback on the project and the thesis.

Thanks to my brother, Petter Myrvold, for proofreading the thesis.

Finally, I would like to express my gratitude to my family for their ever-lasting support throughout my time at NMBU, and to my girlfriend for motivating me and for her ability to put a smile on my face.

Eivind Myrvold
Ås, 15.12.2017

Abstract

Rotor-stator interaction in high-head Francis turbines has led to several failures in recent years. Increasing efficiency demands require design optimization of the turbine components, which may lead to thinner profiles. Not only can the components withstand lower loads; quite often one or more of their natural frequencies are close to that of rotor-stator interaction. Most of the research available has been on runners, while other parts of the turbine are less studied. The main goal of this project was to investigate rotor-stator interaction in a Francis turbine guide vane in order to evaluate why resonance has not been a problem in this part of the turbine.

The finite element method was used for the structural analyses in this thesis. Modal analyses in air and water were conducted to evaluate the mode shapes and natural frequencies of the guide vane. As expected, a torsional mode showed a natural frequency close to the blade passing frequency. The distance to resonance in air was 4.7%. The natural frequency of the same mode in water was found to be 155.7 Hz as the added mass effect led to an 11% reduction. The distance to resonance in water was 6.5%.

A harmonic response analysis was performed by applying a pressure field on the guide vane blade. The results showed that the torsional mode was excited, and the resulting displacement amplitude was 0.14 mm on the guide vane leading edge. The rotor-stator interaction caused a torque of 4 616 Nm acting on the guide vane. Comparison was made with the friction moment caused by friction in the bearings. The bearings above and below the blade caused a combined friction moment of 5 150 Nm, indicating that the guide vane does not slide in the bearings. A modal analysis modelling the guide vane as fixed in these bearings showed that the natural frequency of the mode was no longer close to resonance. This is believed to be the reason why resonance problems have not been experienced for the guide vanes.

Damping calculations were performed using CFX. The goal was to evaluate the influence of damping if the torque does indeed overcome friction. The guide vane profile was forced to vibrate in the mode shape and frequency found for the first mode of the modal analysis in air. The displacement amplitude was set to 0.14 mm according to the results of the harmonic response analysis. Two methods of calculating the damping were used: one is the pre-defined aerodynamic damping option, while the other makes use of the wall work density on the blade. The calculated damping was found to be around 3-3.5% depending on the mesh and method of calculation.

Sammendrag

Flere høytrykks Francisturbiner har hatt problemer forbundet med rotor-stator interaksjon de siste årene. Et stadig press på å forbedre effektiviteten i slike turbiner medfører tynnere profiler og dermed strukturer som tåler mindre belastning. I tillegg observeres det at egenfrekvensen til turbinene ofte korrelerer med lastfrekvenser forbundet med rotor-stator interaksjon. Mye av forskningen på området er gjort på selve løpehjulene, mens færre studier er gjort av andre turbindeler. Hovedmålet i dette prosjektet har vært å undersøke rotor-stator interaksjon i ledeskovlene i en høytrykks Francisturbin.

De strukturelle beregningene i oppgaven er gjort ved bruk av elementmetoden. Det ble gjennomført modalanalyser i luft og vann for å finne formen og egenfrekvensen til de ulike svingemodene. Som forventet var egenfrekvensen til en torsjonsmode nær frekvensen løpehjulsskovlene passerer ledeskovlene med. I luft ble avstanden til resonans beregnet til 4.7%. For beregningene i vann bidro effekten av «added mass» til å senke denne egenfrekvensen til 155.7 Hz, en 11% reduksjon. Avstanden til resonans i denne beregningen var 6.5%.

Det ble så utført en harmonisk responsanalyse ved å påføre et trykkfelt på bladet av ledeskovlen. Resultatene viste at torsjonsmoden funnet i modalberegningen ble eksitert av trykkfeltet fra rotor-stator interaksjonen. Dette resulterte i en deformasjonsamplitude på 0.14 mm på ledeskovlens innløpskant. Det ble også funnet et dreiemoment med en amplitude på 4 616 Nm på ledeskovlen. Friksjonsmomentet i lagrene ble vist å være 5 150 Nm. Resultatene tyder dermed på at det dynamiske momentet som virker på ledeskovlen ikke er stort nok til å overkomme friksjonen, og at ledeskovlen ikke vil gli i lagrene som først antatt. En ny modalberegning ble kjørt med fastholdning i lagrene, hvor det ble vist at egenfrekvensen til torsjonsmoden ikke lenger er i faresonen for å forårsake resonans. Dette antas å være grunnen til at det ikke har oppstått resonansproblemer med ledeskovlene i turbinen.

Det har også blitt gjennomført dempingsberegninger ved bruk av CFX. Hensikten med dette var å evaluere hvilken rolle dempingen har dersom friksjonen ikke skulle være stor nok til å fastholde ledeskovlen. Profilet til ledeskovlen ble påtvunget bevegelse med svingemoden funnet i modalberegningen, med en amplitude på 0.14 mm på innløpskanten. Dempingen ble så beregnet på to måter: Med den innebygde «aerodynamic damping»-funksjonen i CFX og ved hjelp av «wall work density». Dempingen ble funnet til å være i området 3-3.5% avhengig av hvilket mesh som ble benyttet og hvilken metode dempingen beregnes med.

Contents

Acknowledgements **I**
Abstract **III**
Sammendrag **V**
Contents **VII**
List of tables **VIII**
List of figures **IX**
Nomenclature **X**

1. **Introduction** **1**
   1.1 Previous work ... 3
2. **Project description** **5**
   2.1 Problem statement ... 5
   2.2 Goals and objectives ... 6
   2.3 Limitations and assumptions ... 6
3. **Theoretical background** **7**
   3.1 Simple harmonic motion ... 7
   3.2 Damping and resonance ... 9
   3.3 Flow phenomena ... 12
   3.4 Hydro turbines ... 15
   3.5 Excitation forces in Francis turbines ... 18
   3.6 Fluid-structure interaction ... 20
   3.7 Structural numerical modelling ... 21
   3.8 Computational fluid dynamics theory ... 25
4. **The turbine** **28**
5. **Structural analyses** **29**
   5.1 General settings ... 29
   5.2 Modal analyses ... 31
   5.3 Harmonic response analysis ... 34
   5.4 Static structural ... 37
   5.5 Modal analysis with fixed support ... 39
   5.6 Structural analyses conclusions ... 40
6. **CFX analyses** **41**
   6.1 General settings ... 41
   6.2 Steady state analysis ... 43
   6.3 Transient analyses ... 44
   6.4 CFX conclusions ... 50
   6.5 Damped vs undamped harmonic response analysis ... 51
7. **Discussion and conclusion** **53**
   7.1 General discussion ... 53
   7.2 Notes on the numerical modelling ... 54
   7.3 Conclusion ... 55

References **57**

List of tables

Table 1: Turbine data 28
Table 2: Size of the acoustic domain 30
Table 3: Mesh information for modal in air analysis 31
Table 4: First 6 natural frequencies of guide vane in air 32
Table 5: Modal acoustics mesh information 33
Table 6: Natural frequencies of the first 6 modes 33
Table 7: Mesh statistics for the harmonic response analysis 35
Table 8: Harmonic response analysis frequency settings 35
Table 9: Mesh statistics for the static structural analysis 38
Table 10: Results from static structural analysis 38
Table 11: Computed friction moment based on static bearing forces 39
Table 12: Natural frequencies of the first 6 modes for analysis with fixed support 40
Table 13: General mesh settings used in CFX analyses 43
Table 14: Number of inflation layers around guide vane profile and covers 44
Table 15: Mesh quality statistics 44
Table 16: Boundary settings for guide vane profile 45
Table 17: Transient blade row model settings 45
Table 18: Results from damping versus amplitude study 50
Table 19: Results from damped and undamped harmonic response analysis 51

List of figures

Figure 1: World electricity production in 2015 by fuel [2] 1
Figure 2: Installed capacity of renewable energy sources and combined growth rate [3] 1
Figure 3: Mass-spring system for simple harmonic motion 7
Figure 4: Damped oscillation curve showing the underdamped motion and corresponding amplitude 9
Figure 5: Visualization of resonance and damping effects on amplitude [20] 11
Figure 6: Portion of flow in a tube as a control volume 12
Figure 7: Sectioned pipe with streamline illustrating Bernoulli’s principle 13
Figure 8: Francis turbine overview with components [23] 15
Figure 9: Pressure and suction side of a guide vane [26] 17
Figure 10: The effects of runner vanes and guide vanes on the flow field [31] 18
Figure 11: Vortex street produced by flow over cylinder at Re = 140. 19
Figure 12: Names of the guide vane parts used in the thesis 28
Figure 13: Work flow to evaluate the dynamic response 29
Figure 14: Acoustic domain size parameters 30
Figure 15: Guide vane boundary conditions (left) and mesh (right) 31
Figure 16: Mode shape of the first mode in air 32
Figure 17: Modal acoustics mesh 32
Figure 18: Mesh sensitivity analysis for the natural frequency of the first mode 33
Figure 19: Imported pressure for harmonic response analysis 34
Figure 20: Mesh sensitivity of harmonic response analysis 35
Figure 21: Harmonic response analysis stress amplitude spectrum 36
Figure 22: Plot of maximum principal stress amplitude 36
Figure 23: Deformation plot at 166 Hz 37
Figure 24: Mapped static pressure 38
Figure 25: Visualization of guide vanes around the turbine 42
Figure 26: Guide vane opening angle 42
Figure 27: CFX boundary conditions 42
Figure 28: Mesh convergence plots for steady state analysis 43
Figure 29: Plot of calculated damping for different timesteps. 46
Figure 30: Comparison of damping from monitor and wall work density calculations 47
Figure 31: Plot of analysis run time versus number of timesteps per period 47
Figure 32: Velocity plot around guide vane profile. For visualization 48
Figure 33: CFX aerodynamic damping monitors. 48
Figure 34: Rms residuals of CFX analysis with 144 timesteps per period and mesh 5 49
Figure 35: Plot of wall work density averaged over the last period 50
Figure 36: Frequency response of damped and undamped models 51

Nomenclature

Abbreviations

BEP	Best-efficiency point
CFD	Computational Fluid Dynamics
DOF	Degree of Freedom
FEM	Finite element method
FSI	Fluid-structure interaction
NMBU	Norwegian University of Life Sciences
RANS	Reynolds averaged Navier-Stokes equations
RSI	Rotor-stator interaction

Roman letters

Symbol	Description	Unit
A	Area	m^2
B, C	Amplitude	m
E	Total mechanical energy	J
F	Force	N
K	Kinetic energy	J
M	Moment	Nm
Q	Q factor	$-$
T	Period	s
U	Potential energy	J
W	Work	J
Z_{r}, Z_{gv}	Number of runner blades, number of guide vanes	$-$
a	Acceleration	m/s^2
b	Damping constant	kg/s
c	Speed of sound	m/s
f	Frequency	Hz
fb, fgv	Blade passing frequency, guide vane frequency	Hz
g	Gravitational constant	m/s^2
h, l, w	Size parameters of acoustic domain	m
k	Spring stiffness	N/m
m	Mass	kg
n_r	Runner rotational speed	RPM
p	Pressure	Pa
q_i	Generalized coordinate	$-$
q_0	Scaling factor	$-$
r	Radius	m
t	Time	s
u	Displacement	m
u_t	Friction velocity	
v	Velocity	m/s
y	Displacement in y direction	m
y^+	Non-dimensional wall distance	
z	Elevation	m

Greek letters

Symbol	Description	Unit
Ω	Angular frequency	Hz
α	Mass matrix damping proportionality constant	$-$
β	Stiffness matrix damping proportionality constant	$-$
γ	Specific weight	N/m^3
δ	Phase constant, Kronecker Delta function	rad
ζ	Damping ratio	$-$
θ	Displacement phase shift	rad
λ	Wavelength	m
μ	Viscosity	$Pa \cdot s$
μ_{fr}	Friction coefficient	$-$
ν	Kinematic viscosity	m^2/s
ρ	Density	kg/m^3
τ	Time constant, stress tensor	
χ	Inflow angle	$Degrees$
ψ	Force phase shift	rad
ω	Angular frequency	rad/s

Matrices

$[B]$	Acoustic damping matrix
$[C]$	Damping matrix
$[H]$	Acoustic stiffness matrix
$[K]$	Stiffness matrix
$[L]$	Coupling matrix
$[M]$	Mass matrix
$[Q]$	Acoustic mass matrix

Vectors

$\{\ddot{u}(t)\}$	Nodal acceleration vector	m/s^2
$\{\dot{u}(t)\}$	Nodal velocity vector	m/s
$\{u(t)\}$	Nodal displacement vector	m
$\{F(t)\}$	Applied load vector	N
ϕ	Eigenvector representing the mode shape	
$\hat{n}$	Surface normal unit vector	

1. Introduction

The shift from fossil to renewable energy sources is one of the key challenges of our modern society. Global warming with all its negative implications is already upon us, and to mitigate the worst consequences, the need for renewable energy is ever growing. While global energy demand is projected to rise 48% by 2040 (from 2012 levels), electricity generation is expected to rise 69% [1]. Figure 1 shows the sources of energy for electricity production in 2015, of which hydropower counted 16%.

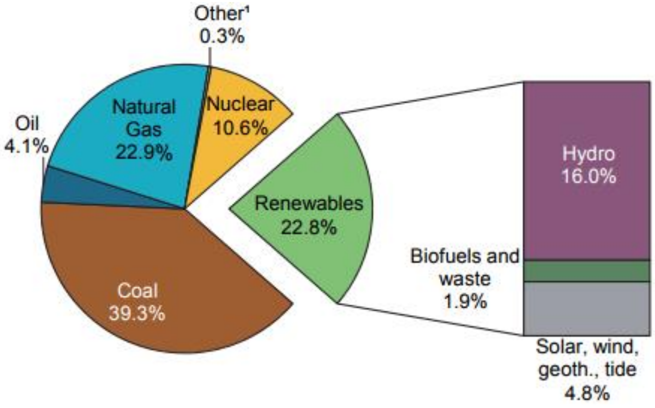

Figure 1: World electricity production in 2015 by fuel [2]

Adding to the expected growth of electricity generation, a high and increasing growth rate of renewable energy for electricity generation can be seen from Figure 2. Drivers for this development include lower cost, more efficient technologies, and political incentives in order to reach the desired greenhouse gas emission reductions.

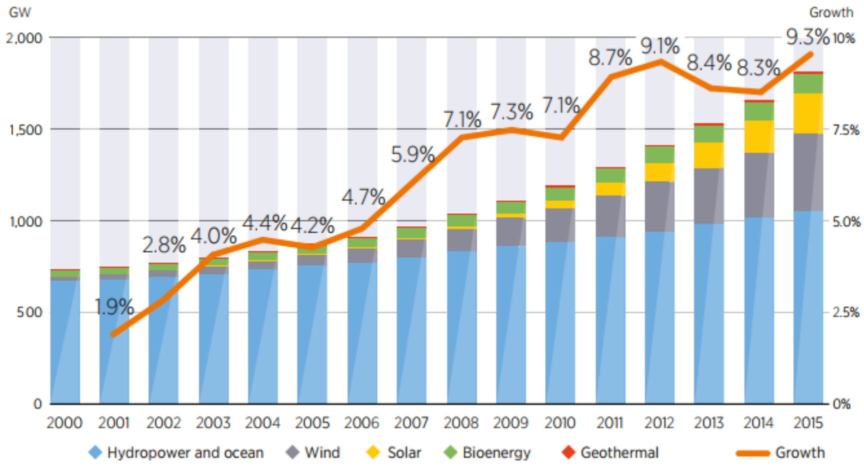

Source: IRENA. 2016b

Figure 2: Installed capacity of renewable energy sources and combined growth rate [3]

Figure 2 also shows that hydropower has by far the largest installed capacity amongst renewables. The average annual growth rate of renewables such as Solar PV and wind, 45.5% and 24% respectively, highly surpass that of hydropower (2.4%) [2]. However both of these grew from much smaller bases. In fact, 2015 was the first year both solar and wind had higher added capacity than hydropower [3]. The continuous technological development of hydropower equipment is clearly of high importance in reaching the global goals for renewable energy production.

Hydropower is considered a highly reliable and flexible source of electricity. The ability to directly store energy in a reservoir reduces the need of additional energy storage. The power output from renewables such as wind and solar may see large variations depending on local weather conditions. Hydropower, on the other hand, is much less sensitive to such variations. Hence, the ability to implement long-term production planning combined with the relative ease of power regulation is a huge advantage of hydropower plants. This will become increasingly important as the switch from fossil to renewable sources implies a larger variability in power output.

The increasing demand on flexibility and output regulation are putting hydropower turbines under more challenging operation schemes. Turbines are more frequently operated further away from the best-efficiency point (BEP), and start/stops happen more often. Combined with increasing demands on optimization of efficiency and weight, this may lead to higher stresses and more severe vibrations in the structure.

The effects can be seen when considering rotor-stator interactions (RSI), which has led to failure of several high-head Francis turbines. One example of this is the Svartisen A1 runner that failed in 2011. High pressure fluctuations are induced each time a runner blade passes a guide vane. If the passing frequency is close to the structure’s natural frequency resonance occurs, and large stresses and amplitudes are induced. Research interest on RSI has increased as a result of the recent failures. However, most focus has been on the runner itself, while other components within the turbine have received less attention. In addition, the effects of hydraulic damping and bearing friction are often neglected. The purpose of this thesis is therefore to evaluate the rotor-stator interaction of a Francis turbine guide vane. In particular it is interesting to evaluate why resonance has not caused the same type of problems in guide vanes as seen in runners.

1.1 Previous work

Several recent runner failures have led to an increased research on dynamic loads in hydraulic turbines. According to Seidel et.al., RSI is the main dynamic load in a high-head Francis turbine [4]. Up to 80% of the dynamic load on a high head runner may be attributed to RSI induced at the guide vane passing frequency. The evaluation of RSI is usually done either by experimental testing or numerical simulations. Because the work in this project is a pure numerical analysis only numerical research is presented. Most of the work is focused on the runners, while very few numerical studies on guide vanes have been published. Articles typically focus either on the added mass effect or evaluation of RSI induced pressures and stresses. More recently a few numerical studies of hydrodynamic damping have been published.

1.1.1 Added mass

In 2007, Liang et al. performed numerical simulations on a Francis turbine model runner to determine the added mass effect [5]. The model was a 1:10 scale runner with 17 runner blades, and by considering rotational periodicity of the structure the authors modelled one sector ($1/17^{th}$) of the turbine. This allows for a much smaller computational model. The calculated results were compared to experiments performed by Rodriguez et al on the same runner [6]. Mode shapes and natural frequencies corresponded well between the numerical and experimental analyses both in air and water. Numerically determined natural frequencies in water were within ± 3.5% of the experimental results. The eigenfrequencies were reduced between 11-38% for different mode shapes, showing clearly that added mass is not the same for all modes.

Rodriguez et al. performed a thorough investigation of the added mass effect in 2012, where the influence of nearby structures were taken into account [7]. The case studied was a cantilever beam. It was shown that the proximity of a solid structure increases the added mass effect. The deviations between the measured and computed natural frequency were quite small, with an average of 2.5% difference.

In 2016, Valentin et al. used a one-way structural-acoustic fluid-structure interaction (FSI) on a Francis turbine to study how the added mass effect is affected by boundary conditions [8]. For the larger radial gaps between the runner and the stator tested, the reduction of the natural frequencies was about 30% compared to that in air. For smaller gaps the added mass effect increased and natural frequencies were reduced even more. No comparison with experimental results was made.

1.1.2 Pressure, stress and damping analyses

In 2000, Avellan et al. compared the results from computational fluid dynamics (CFD) calculations on a model turbine runner with the results of pressure measurements performed using piezo-resistive pressure transducers [9]. The results show good correlation both on the pressure and suction side of the runner blades with the numerical solution slightly overestimating the pressure. The authors make no description of the numerical model other than using the $\kappa - \epsilon$ turbulence model.

Methods to numerically evaluate the natural frequency, mode shape, the dynamic response of a runner due to RSI and damping calculations were presented in 2010 by Hübner et al. [10]. They argue that modelling the added mass effect using acoustic, stagnant fluid elements is sufficient. For damping calculations however, the fluid flow must be modelled. Reasonable correlation is shown between numerical and experimental results for the strain at 16 different locations on a runner vane when Seidel et al. applied similar methods for evaluating the RSI induced stresses in 2012 [4]. The runner used was a 150 rpm high head Francis runner with 15 runner blades and 24 guide vanes. The model was based on a strongly coupled approach, often referred to as 2-way FSI.

Østby et al. performed numerical analyses of pressures and stresses of three high-head Francis turbines in 2016 and compares the results to experimental results on prototype runners [11]. The results at the RSI frequency are reported at around 70% load and full load. Their calculations are able to predict the pressures well, however larger deviations are seen for the stress amplitudes. Damping calculations are also performed for the runners at different power outputs, and the damping ratio increases with increased power output.

In 2017, Gauthier et al. presented an approach to calculate the flow-induced damping of flow over a hydraulic turbine blade [12]. The mode shape and eigenfrequencies are obtained from a modal analysis. Forced oscillatory motion is then applied on the structural boundary. The authors then perform Reynolds averaged Navier-Stokes (RANS) simulations and compute the damping using normalized work done by the structure. The calculated damping seems to converge around 0.14%.

1.1.3 Guide vanes

Not a lot of published numerical studies on guide vanes have been found. The ones found include assessment of leakage flow (i.e. [13],[14]), sediment erosion ([15], [16]) and the added mass effect [17]. To the author's knowledge no study of the dynamic response of the guide vane has been published. Thus, properly evaluating how RSI phenomena affect the Francis turbines would provide useful knowledge to those who design and sell turbine equipment.

2. Project description

2.1 Problem statement

Several recent high-head Francis turbine failures have been linked with resonance. This has increased the interest of determining the dynamic response of hydropower turbines. When designing hydropower turbine equipment such as runners and guide vanes, natural frequency calculations including the “added mass effect” are commonly performed. If the calculated natural frequencies are too close to the loading frequency, the design is modified. However, to the author’s knowledge, little attention has been paid to determine the contribution of damping and friction. More thorough knowledge on how such phenomena affect the structural response may significantly affect how turbine design is performed.

The main objective of this thesis is to investigate rotor-stator interaction in a Francis turbine guide vane in order to evaluate why resonance has not been a problem in this part of the turbine. The analyses are based on actual geometry installed in a large high-head power plant in Norway, supplied by Rainpower Norge AS. The guide vanes of this turbine have a natural frequency close to the blade passing frequency, and resonance is expected. However, the turbine is running smoothly without vibrational problems in the guide vanes. With the specific geometry in mind, the goal of this thesis is to investigate what may be the reason resonance problems are not experienced for this turbine.

Performing such analyses requires knowledge and skills within the fields of structural statics and dynamics, fluid mechanics and vibrations. The first part of this thesis is therefore dedicated to the theoretical background of the problem. A literature study then presents past and present research on relevant topics. Based on the findings in these sections, an assessment of numerical analysis methods will be performed. The preferred method will then be applied to the guide vane for a numerical analysis of its dynamic response.

2.2 Goals and objectives

Main goal

- The main goal of the thesis is to investigate why resonance is not a common problem for Francis turbine guide vanes. Focus is put on how bearing friction and hydrodynamic damping affect the dynamic response of the guide vane.

To achieve this goal, the thesis will have the following objectives:

- Acquire a thorough knowledge of dynamics. Particular focus on the theoretical background for vibrations, hydrodynamic damping and resonance.
- Perform a literature review of previous and ongoing research
- Select appropriate numerical techniques for finite element method (FEM) and CFD analyses
- Perform FEM and CFD analyses
- Continuously evaluate the validity of numerical results
- Make appropriate adjustments to the numerical models according to results found in the analyses

2.3 Limitations and assumptions

The scope of the project is defined by the following limitations:

- Only numerical analyses will be performed
- The numerical analyses will focus solely on one turbine
- The geometry is supplied by Rainpower
- The project does not focus on the guide vane design itself. No changes will be made to the guide vane geometry, neither will any attempt to suggest design changes be made
- Focus is put on trying to evaluate why resonance issues are not seen in guide vanes in the same manner as for runners
- No fatigue calculations will be performed

3. Theoretical background

The purpose of this chapter is to present some of the theoretical foundation that is necessary to understand the problem and work in this project. The first two subchapters present the general vibration theory applied: the concept of simple harmonic motion, damping and resonance. The textbook “Physics for Scientists and Engineers” by Tipler and Mosca [18] has been used to present these basic concepts, with some additions from other physics textbooks. Chapters 3.3 – 3.7 cover the fluids part of the theory: turbulence and the boundary layer, hydraulic turbines, excitation forces and fluid-structure interaction. Fluid dynamics theory is reproduced from Finnemore and Francini’s book “Fluid Mechanics with Engineering Applications” [19]. The final chapters present the theory behind numerical analyses in ANSYS Mechanical and CFX.

3.1 Simple harmonic motion

The concept of simple harmonic motion is useful to gain a general understanding of vibrations. Simple harmonic motion is an oscillating system where the restoring force and acceleration is linearly proportional to the displacement from static equilibrium. A spring-mass system such as in Figure 3 is presented as a case of simple harmonic motion. The spring exerts a restoring force:

$$F_y = -ky \tag{3-1}$$

where k is known as the spring constant (spring stiffness) and y the displacement from static equilibrium. This is commonly known as Hooke’s law. At static equilibrium the spring is already stretched from its unloaded length, exerting a force equal to but opposite of gravity.

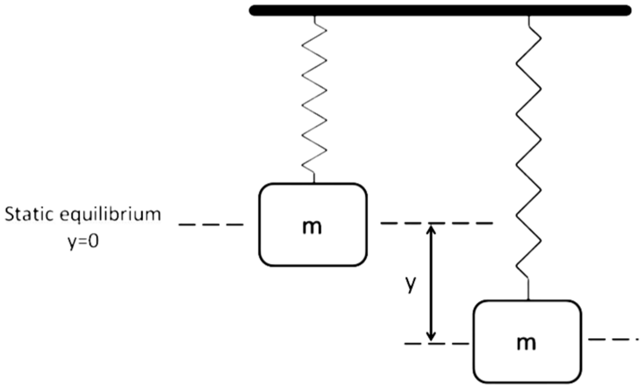

Figure 3: Mass-spring system for simple harmonic motion

Combining Newton’s second law ($F_y = ma_y$) with Hooke’s law gives:

$$-ky = ma_y \tag{3-2}$$

Equation (3-2) can be rearranged for the acceleration:

$$a_y = -\frac{k}{m}y \tag{3-3}$$

The factor $-k/m$ is a system constant that only depends on the spring stiffness and oscillating mass. By defining a system parameter $\omega_0 = \sqrt{k/m}$, equation (3-3) can be rewritten as:

$$a_y = -\omega_0^2 y \tag{3-4}$$

The system parameter ω_0 corresponds to the angular natural frequency of the system. Acceleration is the second order time derivative of position, so that:

$$\ddot{y} + \omega_0^2 y = 0 \tag{3-5}$$

Equation (3-5) is a second order homogenous differential equation with constant coefficients, which has the general solution:

$$y = B\cos(\omega_0 t) + C\,sin(\omega_0 t) \tag{3-6}$$

Here, B and C are the amplitudes of the real and imaginary parts of the solution. The period of such an oscillation is defined as:

$$T = \frac{2\pi}{\omega_0} \tag{3-7}$$

The period of an oscillation is the reciprocal of the frequency, $T = 1/f$. The natural frequency of the system can then be found from equation (3-8):

$$f_0 = \frac{1}{2\pi}\sqrt{\frac{k}{m}} \tag{3-8}$$

This is the frequency at which the mass would oscillate around static equilibrium if given an initial displacement and then released. The total mechanical energy (E) of such a system is constant and equal to the sum of kinetic (K) and potential (U) energy. It can be shown that the mechanical energy is proportional to the square of the amplitude:

$$E = U + K = \frac{1}{2}kB^2 \tag{3-9}$$

The average values of kinetic and potential energy over one or several whole cycles is:

$$U_{av} = K_{av} = \frac{1}{2}E \tag{3-10}$$

3.2 Damping and resonance

3.2.1 *Damping*

A system is said to be damped when energy is dissipated. Energy may be dissipated by several means, including friction, viscous damping, hysteresis losses and wave propagation. Dry friction is often modelled as Coulomb friction, where the friction force depends on the friction coefficient between two objects in contact, and the net force acting along the plane of contact. Hysteresis, on the other hand, refers to the internal friction in a structural member. It is related to the resistance to motion of particles within a material. Viscous damping will be the focus in this thesis, and the following discussion is based on this type of damping.

If the spring-mass system in Figure 3 was put into motion then left to itself, the amplitude would be reduced at each cycle, and the mass would eventually come to rest. If the mass body in the spring-mass system considered was submerged in water, frictional forces would increase and the mass comes to rest after fewer oscillations than in air. Such behavior, where the amplitude is reduced each cycle, is referred to as an underdamped motion. The viscous damping force exerted in an underdamped system can be expressed as:

$$F_d = -bv \tag{3-11}$$

This is a case of linear damping, where b is referred to as the damping constant. Using $v = dx/dt$ combined with Newton’s second law the differential equation for a damped oscillator can be obtained:

$$m\ddot{y} = -b\dot{y} - ky \tag{3-12}$$

For an underdamped motion the solution to equation (3-12) is:

$$y = B_0 e^{-(b/2m)t} \cos\,(\omega' t + \delta) \tag{3-13}$$

The resulting displacement can be plotted over time as in Figure 4. The plot clearly shows how the amplitude, and thus energy, decreases with each cycle.

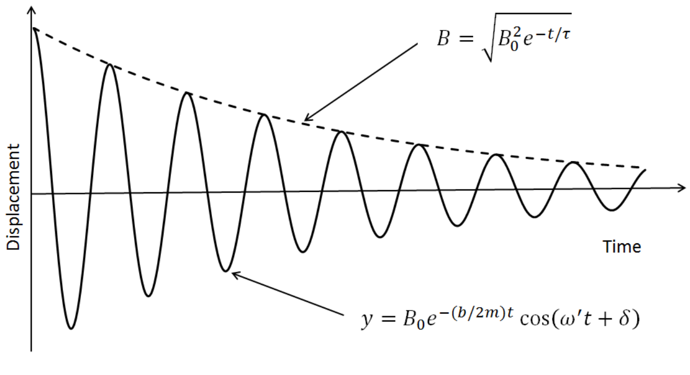

Figure 4: Damped oscillation curve showing the underdamped motion and corresponding amplitude

The time constant τ is the time it takes for the energy reduction to change by a factor of e^{-1} and can be expressed as:

$$\tau = \frac{m}{b} \tag{3-14}$$

This becomes useful when considering the Q factor of oscillating systems. The Q factor is related to the amount of energy dissipated in each cycle due to weak damping friction losses:

$$Q = \frac{2\pi}{(\Delta E/E)} = \omega_0 \tau \tag{3-15}$$

A high Q factor describes a weakly damped system where energy is dissipated slowly. Conversely, a system where energy dissipates rapidly has a low Q factor.

Rearranging equation (3-12) and using $\omega_0 = \sqrt{k/m}$ the differential equation can be written as

$$\ddot{y} + \frac{b}{m}\dot{y} + \omega_0^2 y = 0 \tag{3-16}$$

Critical damping is the case where the amplitude reaches zero the fastest possible way, and occurs when $b/m = 2\omega_0$. The damping ratio ζ is defined as the ratio of actual damping, in this case b/m, to the critical damping:

$$\zeta = \frac{b/m}{2\omega_0} \tag{3-17}$$

The differential equation for damped oscillations undergoing simple harmonic motion can then be written as:

$$\ddot{y} + 2\zeta\omega_0\dot{y} + \omega_0^2 y = 0 \tag{3-18}$$

The angular frequency of a damped oscillation is related to the natural angular frequency by:

$$\omega' = \omega_0 \sqrt{1 - \left(\frac{b}{2m\omega_0}\right)^2} = \omega_0\sqrt{1 - \zeta^2} \tag{3-19}$$

In the case of weak damping, $b \ll 2m\omega_0$, and the difference between the undamped and damped angular frequencies is considered negligible. This means that for weakly damped systems it is often acceptable to assume that the natural frequency of a structure is not affected by damping.

3.2.2 Resonance

An oscillating system is said to be driven when mechanical energy is added in a cyclic motion. The resulting amplitudes mainly depend on three factors; the amplitude and frequency of the driving force, of which the frequency effects are less straightforward, and damping. If the driving frequency is close to the natural frequency of the system, large amplitudes occur. This particular behavior is referred to as resonance. The amplitude in two similar systems with different damping will differ more close to resonance, as seen in Figure 5. In other words, damping effects play a larger role for systems driven at a frequency close to the natural frequency.

The concept of resonance can be visualized by looking at a swing. An initial push would put the swing into motion, and the person would swing back and forth as a pendulum in the natural frequency of the system. Pushing in the same frequency as this motion will make the swing go higher, while an attempt to push in a different frequency will be less efficient. In most structural applications however, resonance is unwanted. The added energy and large amplitudes may lead to plastic deformations, crack growth or even structural failure.

For oscillations with a harmonically varying driving force, the system can be described by:

$$\ddot{y} + \frac{b}{m}\dot{y} + \omega_0^2 y = F_0 \cos \omega t \tag{3-20}$$

where F_0 is the amplitude and ω the angular frequency of the driving force. The general solution to equation (3-20) is:

$$y = B \cos(\omega t - \delta) \tag{3-21}$$

and the amplitude for such a system is:

$$A = \frac{F_0}{\sqrt{m^2(\omega_0^2 - \omega^2)^2 + b^2\omega^2}} \tag{3-22}$$

For a system with very small damping $(\boldsymbol{b} \approx \mathbf{0})$, the amplitude goes towards infinity as $\boldsymbol{\omega} \to \boldsymbol{\omega_0}$. On the other hand, if $\boldsymbol{\omega_0} - \boldsymbol{\omega}$ is large, the term $\boldsymbol{b^2\omega^2}$ is negligible and damping effects can be ignored. The effects of resonance and damping close to the natural frequency can be seen in Figure 5.

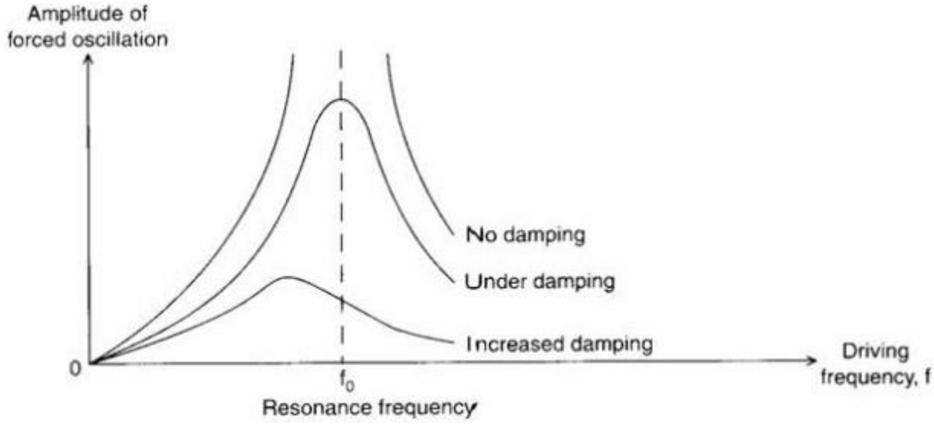

Figure 5: Visualization of resonance and damping effects on amplitude [20]

3.3 Flow phenomena

3.3.1 Governing equations

Continuity equation

The continuity equation is the statement of conservation of mass in fluid dynamics. For a control volume such as the one shown in Figure 6 the continuity equation states that the mass inflow is equal to the sum of mass outflow and accumulation within the control volume. For a steady state flow the mass accumulation equals zero and the continuity equation can be expressed as:

$$\rho_1 A_1 v_1 = \rho_2 A_2 v_2 \tag{3-23}$$

For incompressible fluid the density is constant and Equation (3-23) reduces to:

$$A_1 v_1 = A_2 v_2 \tag{3-24}$$

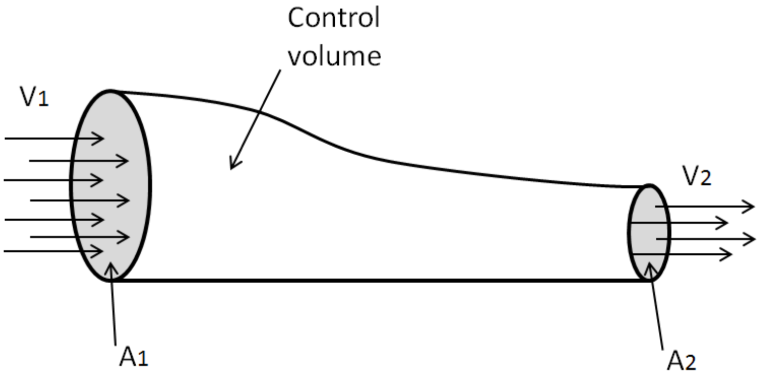

Figure 6: Portion of flow in a tube as a control volume

Bernoulli’s equation

Conservation of energy is governed by Bernoulli’s equation. This equation relates three types of energy in a flow: pressure head, potential energy and kinetic energy. Several assumptions are made when considering Bernoulli’s equation:

- Ideal flow, so viscosity is neglected
- Flow is steady state
- The equation is only valid along streamlines, not across
- Fluid is incompressible
- No energy is added or removed along a streamline.

The energy is often reported on a per unit weight basis, as in Equation (3-25):

$$\frac{p}{\gamma} + z + \frac{v^2}{2g} = constant\ along\ streamline \tag{3-25}$$

Here, p denotes the pressure, γ is the specific weight of the fluid, z is the elevation, v the flow velocity and g is the gravity constant. An illustration of the Bernoulli principle is given in Figure 7, where the sum of pressure, potential and kinetic energy is the same at points 1 and 2 which lie on the same streamline. Bernoulli's equation can be expanded to include head losses for viscous flow.

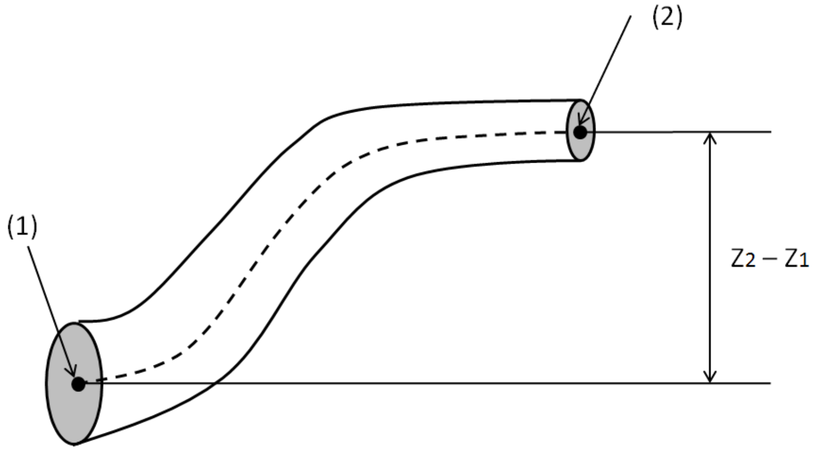

Figure 7: Sectioned pipe with streamline illustrating Bernoulli's principle

Navier-Stokes

The general solution to flow problems is governed by the Navier-Stokes equations. They include both surface and body forces that act on the fluid, such as friction, gravity and pressure forces. The equations state that the sum of body and surface forces are equal to the change of momentum in the flow. The full Navier-Stokes equations form the basis of computational fluid dynamics (CFD).

$$-\frac{\partial p}{dx}+\mu\left(\frac{\partial^2 u}{\partial x^2}+\frac{\partial^2 u}{\partial y^2}+\frac{\partial^2 u}{\partial z^2}\right)=\rho\left(\frac{\partial u}{\partial t}+u\frac{\partial u}{\partial x}+v\frac{\partial u}{\partial y}+w\frac{\partial u}{\partial z}\right) \tag{3-26}$$

$$-\frac{\partial p}{dy}+\mu\left(\frac{\partial^2 v}{\partial x^2}+\frac{\partial^2 v}{\partial y^2}+\frac{\partial^2 v}{\partial z^2}\right)=\rho\left(\frac{\partial v}{\partial t}+u\frac{\partial v}{\partial x}+v\frac{\partial v}{\partial y}+w\frac{\partial v}{\partial z}\right) \tag{3-27}$$

$$-\rho g-\frac{\partial p}{dy}+\mu\left(\frac{\partial^2 w}{\partial x^2}+\frac{\partial^2 w}{\partial y^2}+\frac{\partial^2 w}{\partial z^2}\right)=\rho\left(\frac{\partial w}{\partial t}+u\frac{\partial w}{\partial x}+v\frac{\partial w}{\partial y}+w\frac{\partial w}{\partial z}\right) \tag{3-28}$$

On the left side of the equation the term ρg denotes the gravity force, the ∂p terms the pressure forces and the μ terms the frictional forces. The right side expresses the rate of change of momentum.

3.3.2 Turbulence

The two main types of flow are laminar and turbulent flow. In laminar flow particles move in straight lines along the direction of flow. Turbulent flow is different in that both the velocity and direction of the flow fluctuates at any point. These fluctuations are caused by eddies that break down into smaller eddies and eventually dissipate due to viscous (laminar) shear. This causes a mixing of fluid particles and dissipates energy more rapidly than viscous shear only. Turbulent flow is highly irregular and typically shows no particular flow pattern. The flow in a hydro turbine is highly turbulent.

3.3.3 Boundary layer

The boundary layer concept is useful for flows in pipes, ducts and around immersed objects. By assuming non-slip motion, fluid particles attach to the walls and are considered stationary relative to the wall. For fully developed laminar flow the velocity increases gradually moving away from the wall, forming a velocity profile with maximum velocity in the middle of the pipe. However, for turbulent flow the boundary layer consists of a viscous sublayer close to the wall and a turbulent boundary layer further from the wall. The turbulent boundary layer may interfere with the viscous sublayer, and the flow here is not truly laminar. The viscous sublayer is usually extremely thin but the steep velocity profile enhances viscous effects. Further away, in the turbulent boundary layer, turbulent shear stress dominates. A transition zone exists between the viscous sublayer and the turbulent boundary layer where both viscous and turbulent shear is present.

The same type of boundary layer is seen when considering flow around immersed objects. Flow around immersed objects induces two types of forces, drag and lift. The drag force can be split into friction drag and pressure drag. To lower the pressure drag objects are often streamlined. However, this increases the effective surface area and friction drag increases. The boundary layer may separate from the body in the case of a steep pressure gradient. Backflows then occur behind the point of separation, and the region of disturbed flow is referred to as the turbulent wake. The velocity in the developed eddies in the wake is high, thus, pressure is low. This pressure difference between the leading and trailing edge of an object is what is called the pressure drag.

3.4 Hydro turbines

There are two main categories of water turbines: impulse and reaction turbines [21]. In an impulse turbine the hydrodynamic pressure is converted to kinetic energy through a nozzle. Water is discharged from the nozzle into air forming a jet stream. The free jet is directed tangentially at the runner buckets where the water changes direction and is slowed, causing a change of momentum. The resulting force on the turbine blade does work as the runner rotates and kinetic energy is transferred from the water to the runner. Impulse turbines are typically used for high head applications with low flow rates, and have a high efficiency over a wide operating range. The most common impulse turbine is the Pelton turbine.

In a reaction turbine, pressurized water flows over the turbine blades. Both the kinetic energy of the water and the hydraulic pressure transfers energy to the runner. As opposed to an impulse turbine the flow is not injected as a jet stream, and the potential-to-kinetic energy conversion happens gradually through the turbine. Reaction turbines must therefore be encased, fully submerged and fitted with a draft tube discharge. Several types of reaction turbine runners exist, and reaction turbines can typically be used for a wide range of flow rates and heads. The most common reaction turbines are the Francis and Kaplan turbine.

3.4.1 Francis turbines

The work in this thesis is based on the geometry of a high-head Francis turbine. The main components of a Francis turbine are presented below to give the reader a better understanding of the governing geometry. The Francis turbine is the most common water turbine worldwide as it covers a large range of heads (10-650 m) and power outputs (10-750 MW) [22].

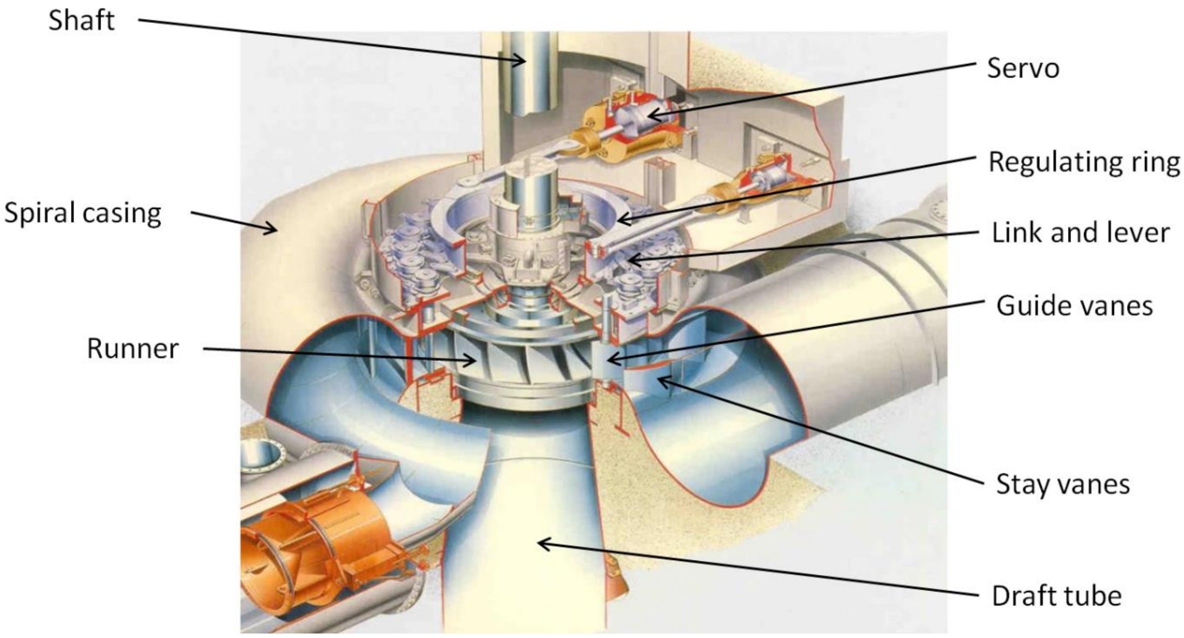

Figure 8: Francis turbine overview with components [23]

- ***Spiral casing:*** Water is distributed around the Francis runner through a spiral casing connected to the penstock. Equal distribution to all stay vanes is desirable, and therefore the cross sectional area of the spiral casing is reduced around the perimeter. This ensures that the load on the runner is as symmetric as possible.

- ***Stay vanes:*** Fixed stay vanes are evenly spaced around the circumference to align parts of the flow with the guide vanes, thereby diverting parts of the flow. The spiral casing and stay vanes together distribute the flow around the runner. Stay vanes are connected to an upper and lower ring and together form what is referred to as the stay ring.

- ***Guide vanes:*** The flow discharge and direction to the runner is controlled by the guide vanes, thereby controlling the power output. They are pivoted and can be rotated to the appropriate opening angle. The guide vanes are supported by shaft bearings connected to the upper and lower cover as well as the governing ring which is used to rotate the guide vanes.

- ***Runner:*** The runner is the entity that converts the hydraulic energy into rotational mechanical energy. It is made up of runner vanes evenly spaced around the runner. The vanes attach to the crown (upper) and band (lower). Water enters the runner radially and is discharged axially. Runner design is mainly focused on increasing turbine efficiency, although structural and manufacturing considerations are also important.

- ***Draft tube:*** The draft tube works as the connection between the runner and the outlet gate. It typically consists of a cone, an elbow and a diffuser. The cross section is gradually increased to recover pressure energy by slowing down the water flow.

- ***Turbine covers:*** The upper and lower cover are structural members designed with high stiffness to prevent large deflections and consequent gaps between guide vane ends and the cover plates. They also function as support for the guide vane shaft bearings.

- ***Seals:*** To minimize leakages in the turbine seals are employed between the runner and the covers. As leakages decrease turbine efficiency these seals help avoiding unnecessary losses.

- ***Regulating ring and servo mechanism:*** The guide vanes attach to the regulating ring through a lever and link. By using a regulating ring all guide vanes are regulated using the same mechanism and the pitch angle will be the same all around the turbine. The regulating ring is operated by a servomotor through an arm controlling the angular pitch. The static pressure on the guide vane blade is large enough that the mechanism is self-closing.

3.4.2 Guide vanes

The guide vanes make up the adjustable part of the distribution mechanism in the Francis turbine. The stay vanes and spiral casing ensure even distribution around the perimeter of the turbine, while the guide vanes control the magnitude and direction of flow. As water flows along the guide vane it is accelerated and pressure energy is converted into kinetic energy [24]. Water velocities at the guide vane exit may reach the point of 50% conversion of hydraulic head, and this is often where the velocity is highest throughout the turbine [25]. The guide vane blade is typically in the shape of a hydrofoil to ensure as little flow disturbance as possible. However, several unsteady phenomena may occur such as rotor stator interactions, cross flows from clearance gap leakages, flow distortion due to pressure gradients, and wakes.

Under operation, one side of the guide vane blade faces the spiral casing while the other faces the runner. As explained by Antonsen, two points on the same chord length of the guide vane lie on different radii, shown in Figure 9 [26]. At point 1 the flow has not yet been restricted between two guide vane profiles. At point 2 however, flow is restricted to a smaller channel. It follows from the continuity equation that the flow will have a higher velocity at point 2. According to Bernoulli’s equation the pressure in the fluid will be lower at this point. This means that the guide vane will have a pressure side and a suction side.

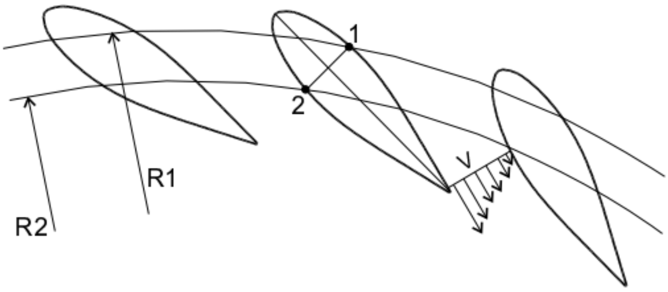

Figure 9: Pressure and suction side of a guide vane [26]

3.5 Excitation forces in Francis turbines

Several time dependent flow induced loads are present in a Francis turbine. Operating at the best efficiency point, the dominating effect is rotor-stator interaction [27]. RSI is believed to be the reason several high-head Francis turbines have failed in recent years, exemplified by the Sønnå Høy failure believed to be caused by resonance induced high stresses in the runner vane [28]. Other time dependent flow phenomena that may affect the turbine include draft tube vortex rope, Von Karman vortex shedding, flow separation and cavitation [29].

3.5.1 Rotor-stator interactions

The RSI effects are caused by pressure fluctuations caused by the relative motion between the turbine rotor and stator. More precisely, two different phenomena causing flow field distortion are present [30]: As the runner rotates, water at the runner inlet is continuously displaced by the runner vanes. Meanwhile the flow on the pressure and suction side of the guide vane has different velocities which causes wakes at the trailing edge. The inflow also has a non-uniform velocity distribution. Leakage flows due to the pressure difference on the pressure and suction side may also cause vortices [24]. The RSI effects are visualized in Figure 10. The figure shows how both the runner vanes and guide vanes affect flow the flow pattern in the vaneless space between the rotor and stator and combine for a cyclic flow field distortion.

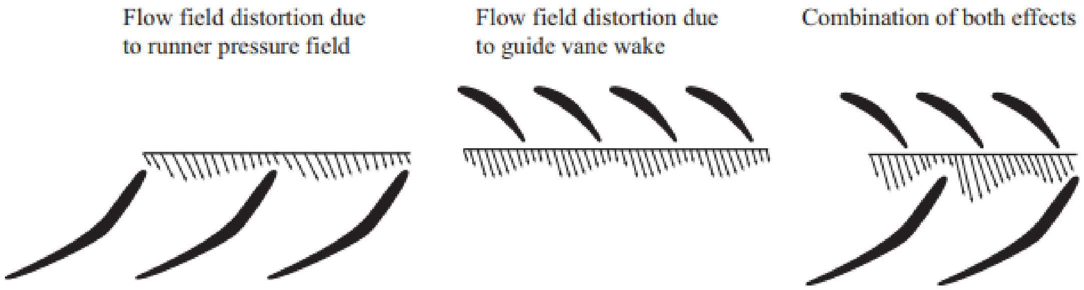
Flow field distortion due to runner pressure field
Flow field distortion due to guide vane wake
Combination of both effects

Figure 10: The effects of runner vanes and guide vanes on the flow field [31]

According to Qian (2008) the RSI effect is the most important source of unsteadiness in the turbine [30]. Depending on what is chosen as the reference frame the rotor-stator interactions are observed at either the blade passing frequency or guide vane passing frequency.

A fixed speed runner rotates at a set number of revolutions per minute, n_r (RPM). If the rotor (runner) is chosen as reference frame each runner vane passes a guide vane at the guide vane frequency:

$$f_b = \frac{Z_{gv} n_r}{60} \tag{3-29}$$

Where Z_{gv} = number of guide vanes.

On the other hand, if the stator is chosen as reference, each guide vane is passed by a runner vane at the blade passing frequency

$$f_{gv} = \frac{Z_r n_r}{60} \tag{3-30}$$

Where Z_r = number of runner blades.

3.5.2 *Von Karman vortex shedding*

Shedding of Von Karman vortices is typically observed when dealing with flow over bluff bodies, but may also appear when studying flow over streamlined bodies with blunt trailing edges [30]. Vortex shedding occurs when flow around a structure separates due to an adverse pressure gradient. This causes the vortices to detach from the structure and form vortex street, as seen for a flow over a cylinder in Figure 11. Low-pressure vortices are shed periodically from either side of the structure resulting in an oscillating pressure field. The frequency at which vortices are shed is called the vortex shedding frequency.

Several factors including trailing edge shape, boundary layer thickness and degree of turbulence affect the frequency of vortex shedding [26]. In addition, the angle of attack may cause early separation and consequently a stalling flow. In a Francis turbine, Von Karman vortex shedding is most commonly seen in stay vanes as they typically have more blunt trailing edges than guide vanes.

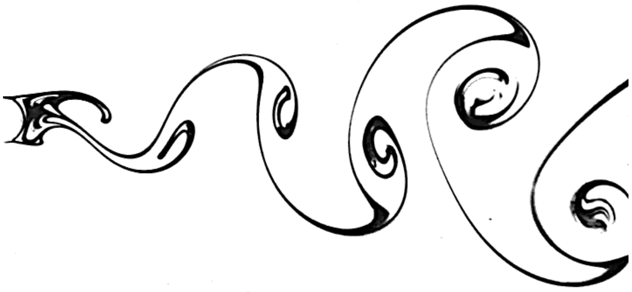

Figure 11: Vortex street produced by flow over cylinder at Re = 140. Photograph by Sadatoshi Taneda, adapted from [32].

3.5.3 *Flutter*

Flutter happens when the motion of a body increases the hydrodynamic force, causing positive feedback. It is a type of self-excited vibration where a steady flow produces an oscillating response of a structure. Flutter has caused catastrophic structural failures, for example at the Tacoma Narrows Bridge collapse [33] and for several airplane crashes [34]. In hydrodynamics, flutter is a result of fluid-structure interaction of hydrodynamic forces and the elastic deformation of a structure, similar to that of aeroelasticity.

3.5.4 Draft tube vortex rope

A vortex rope may be observed by the runner outlet and in the draft tube when operating Francis turbines at part load [30]. The cavitating vortex rope appears when the swirling flow in the draft tube breaks down [35]. Due to the scope of this thesis no detailed study of vortex rope is performed as it is a part load phenomenon observed at the runner exit and draft tube.

3.6 Fluid-structure interaction

As the name implies, fluid-structure interaction is the study of systems where a fluid flow interacts with an elastic structure. The assumption is that the motion of a structure is affected by the flow field, and that again may change the flow. When solving FSI problems it is not sufficient to solve the dynamics of the structure and fluid separately as they are expected to affect each other. This means FSI analysis require multiphysics coupling of the fluid and structure laws of motion.

Two general approaches are available for FSI analyses [36]: A monolithic approach considers both the fluid and structural system in the same mathematical formulation. This means one set of equation that describes both domains are developed. On the other hand, a partitioned approach allows separate computations of the fluid and structure domains. This approach depends on interface information being transferred between the two models.

Fluid-structure interaction analyses based on the partitioned approach may be either 1-way or 2-way FSI. 1-way FSI is typically used when structural deformations are small and the flow disturbance is considered small [37]. In this approach the pressure and temperature distributions are calculated using CFD, then applied as loads to the structure. The structural deformation and corresponding stresses are then computed without any change to the flow field. On the other hand, a 2-way FSI relies on the continuous feedback between the systems. At each timestep the loads from the CFD are transferred to the structure, while structural deformations are transferred back from the FEM analysis.

3.7 Structural numerical modelling

3.7.1 Finite element modelling

The finite element method is used to perform the structural analyses in this project. The finite element method is a numerical method that is used to discretize continuous systems in order to generate an approximate solution [38]. In FEM analyses the structure is divided into a discrete set of elements, with nodes in each corner that connects the elements. Some element types also have nodes along the perimeter. The equations of motion are then solved for all degrees of freedom one node at a time for a given a set of boundary conditions. More nodes typically give a better more accurate approximation to the exact solution, but with longer analysis time. Therefore it is important to find a mesh that provides a good enough approximation without excessive computational effort.

3.7.2 Structural analyses

The commercial FEM program ANSYS Mechanical is used for the structural analyses in this project. Based on the virtual work principle the dynamics of a structure is treated as a semi-discrete equation of motion [39]:

$$[M]\{\ddot{u}(t)\} + [C]\{\dot{u}(t)\} + [K]\{u(t)\} = \{F(t)\} \tag{3-31}$$

where:
$[M]$ = the mass matrix of the structure
$[C]$ = the structural damping matrix
$[K]$ = the stiffness matrix of the structure
$\{\ddot{u}(t)\}$ = the nodal acceleration vector
$\{\dot{u}(t)\}$ = the nodal velocity vector
$\{u(t)\}$ = the nodal displacement vector
$\{F(t)\}$ = the applied load vector

Equation (3-31) describes a force equilibrium where the inertial, damping and stiffness forces equal the external forces. For simplicity the time dependency of the nodal vectors are omitted in the following discussion.

3.7.3 Modal analyses

A modal analysis can be used to determine the mode shapes and corresponding frequencies of a structure. The mode shape can be visualized as the shape the structure would deform into – and out of – if excited at its natural frequency. The modes of a structure depend on the mass and stiffness of the components and on the boundary conditions of the problem.

The modal analyses in ANSYS are solved in the frequency domain. A valid model requires:

- Only structural and fluid degrees of freedom (DOFs)
- Constant mass and stiffness effects
- If damping is modelled the damped eigensolver must be used
- No time varying phenomena such as forces, displacements or pressures

The actual damping in a system is often a combination of viscous, Coulomb and hysteresis damping effects. Thus, damping is often a complex phenomenon that is hard to model. In a modal analysis there are two common ways of handling the damping effects:

- Neglect damping effects: $[C] = 0$
- Model damping as linearly proportional to mass matrix, stiffness matrix or both: $[C] = \alpha[M] + \beta[K]$

Here, α and β are the mass and stiffness matrix damping proportionality constants.

Modal analysis in air

Standard modal analysis involves no fluid-structure interaction, and therefore no added mass effect is taken into account. For simplicity it is referred to as analysis in air while the calculations in reality are modelled in vacuum. Damping effects are neglected in the analysis which reduces the system to [40]:

$$[M]\{\ddot{u}\} + [K]\{u\} = 0 \tag{3-32}$$

Assuming that the system is linear, the vibrations will be harmonic and in the form of:

$$\{u\} = \{\phi_i\} \cos \omega_i t \tag{3-33}$$

Where $\{\phi_i\}$ is the eigenvector that represent the mode shape of mode i, and ω_i the corresponding natural angular frequency. By differentiating equation (3-33) twice and substituting into equation (3-32) this becomes:

$$(-\omega_i^2[M] + [K])\{\phi_i\} = \{0\} \tag{3-34}$$

This is true for either $\{\phi_i\} = \{0\}$, which is a trivial solution, or by setting the determinant equal to zero:

$$\left|-\omega_i^2[M] + [K]\right| = 0 \tag{3-35}$$

In a system of n degrees of freedom equation (3-35) can be solved for n values of the eigenfrequency ω. The eigenvectors can be normalized to the mass matrix according to equation (3-36)

$$\{\phi_i\}^T[M]\{\phi_i\} = 1 \tag{3-36}$$

Modal analysis with acoustic elements

The calculation of mode shapes and natural frequencies of a submerged structure can be performed using the ANSYS ACT Acoustics extension. For FSI problems the system is described by the pressure formulation [11]:

$$\left(-\omega^2\begin{bmatrix}\boldsymbol{M} & 0\\ -\rho\boldsymbol{L}^T & \boldsymbol{Q}\end{bmatrix}+j\omega\begin{bmatrix}\boldsymbol{C} & 0\\ 0 & \boldsymbol{B}\end{bmatrix}+\begin{pmatrix}\boldsymbol{K} & \boldsymbol{L}\\ 0 & \boldsymbol{H}\end{pmatrix}\right)\begin{Bmatrix}u\\ p\end{Bmatrix}=\begin{Bmatrix}F\\ 0\end{Bmatrix} \tag{3-37}$$

M, C and **K** are mechanical system matrices, **Q, B** and **H** are acoustic matrices and **L** is the coupling matrix. u and p are the displacement and pressure vectors while F is the external force vector.

Equation (3-37) is only valid for structures submerged in non-flowing water. However, as the speed of sound in water is much higher than the flow velocity, the effect of flowing water is considered negligible. The modal acoustic analysis is also performed using the assumption of negligible damping. This reduces the system to

$$\left(-\omega^2\begin{bmatrix}\boldsymbol{M} & 0\\ -\rho\boldsymbol{L}^T & \boldsymbol{Q}\end{bmatrix}+\begin{pmatrix}\boldsymbol{K} & \boldsymbol{L}\\ 0 & \boldsymbol{H}\end{pmatrix}\right)\begin{Bmatrix}u\\ p\end{Bmatrix}=\begin{Bmatrix}0\\ 0\end{Bmatrix} \tag{3-38}$$

This is an unsymmetric system, thus it requires an unsymmetric solver. The unsymmetric solver is computationally more demanding as the full matrices need to be stored thereby requiring more memory [40].

When dealing with FSI analyses, ANSYS splits elements into three categories:

- Structural elements (displacement DOFs)
- Coupled elements (pressure and displacement DOFs)
- Uncoupled elements (pressure DOF).

For the modal acoustic analysis the model can be generated using shared topology. Using this option, ANSYS automatically detects FSI surfaces and generates a coupled layer. The coupling matrix handles the acoustic pressure applied to the structure. This way coupled elements are treated with four DOFs, while acoustic elements that are not in the coupled layer only have the pressure DOF.

3.7.4 Harmonic response

A harmonic response analysis is suitable for determining the steady state response of a structure to harmonically varying loads. Under the assumption of structural linearity any sustained sinusoidal load produces a harmonic response. For a structure subjected to such loads a harmonic response analysis may provide information to whether forced vibrations may give rise to resonance.

As the analysis only considers harmonic loads, time effects are not present. Thus, the entire response can be described in the frequency domain with frequency and phase the important parameters. The structural response is usually computed at a certain number of frequencies within a range – referred to as a frequency sweep.

Equation (3-31) is the governing equation of motion for the harmonic response analysis as well. The displacements vary harmonically with the same frequency and may be defined as:

$$\{u\} = \left\{u_{max} e^{i\theta}\right\} e^{i\Omega t} \tag{3-39}$$

where
u_{max} = displacement amplitude
θ = displacement phase shift
Ω = imposed angular frequency

Both u_{max} and θ are frequency dependent, meaning they may have different values at each natural frequency. The force vector can be expressed using a similar notation:

$$\{F\} = \left\{F_{max} e^{i\psi}\right\} e^{i\Omega t} \tag{3-40}$$

where
F_{max} = force amplitude
ψ = force phase shift

Both the displacement and force vector can be rewritten as a combination of real and imaginary vectors (subscript 1 and 2 respectively):

$$\{u\} = \left\{\{u_1\} + i\{u_2\}\right\} e^{i\Omega t} \tag{3-41}$$

$$\{F\} = \left\{\{F_1\} + i\{F_2\}\right\} e^{i\Omega t} \tag{3-42}$$

The governing equation can then be rewritten as

$$(-\Omega^2[M] + i\Omega[C] + [K])(\{u_1\} + i\{u_2\}) = \{F_1\} + i\{F_2\} \tag{3-43}$$

Two different solvers are available for this type of analysis:

- **Full solution method**, which solves equation (3-43) directly using a sparse solver. The solution is calculated at each frequency Ω specified in the analysis settings

- **Mode-superposition (MSUP) method**, which calculates the displacement contributions from each mode independently and then superimposes these. The force vector is treated as the sum of time varying nodal forces $\{F_{nd}\}$ and the scaled load vector $s\{F^s\}$ from the modal analysis: [1]

$$\{F\} = \{F_{nd}\} + s\{F^s\} \tag{3-44}$$

---

[1] During a modal analysis applied loads are ignored in the calculation. However ANSYS stores these loads as load vectors that are applied in the downstream harmonic response analysis.

The displacement vector is then computed as:

$$\{u\} = \sum_{i=1}^{n} \{\phi_i\}\, q_i \tag{3-45}$$

where n is the number of modes computed and q_i the generalized coordinates of the mode. The two methods should give the same results if all modes are included and the problem is linear.

3.8 Computational fluid dynamics theory

3.8.1 General CFD theory

Computational fluid dynamics uses numerical methods to solve fluid mechanics problems. ANSYS CFX is used in this thesis to perform the CFD analyses. CFX uses a Finite Volume Method to numerically determine flow characteristics. The CFX workflow consists of a pre-processor, where the simulation is set up, a solver and a post-processor. The solution to a CFD analysis is obtained by solving the mass, momentum and energy conservation equations, often referred to as the Navier-Stokes equations. The instantaneous solution is obtained by solving these equations.

Several approaches are possible when solving turbulent flow and flow near the wall. These include direct numerical simulation (DNS), large eddy simulation (LES), and turbulence modelling using Reynolds averaged Navier-Stokes equations (RANS). The DNS approach requires the flow to be resolved to the smallest eddy scale, and the computational power required for this approach is far too large for practical use. The LES model is based on filtering out eddies of small scales, while the RANS model is a statistical model. RANS modelling is applied in this thesis, where the flow velocity is split into an average component and a fluctuating component. This is referred to as Reynolds decomposition. Solving the mean velocity terms is straightforward; however the fluctuating component gives rise to new terms called Reynolds stresses. These terms are modelled using an additional set of equations, referred to as turbulence models. Flow near the wall can be modelled using the scalable wall function that uses a logarithmic profile to approximate the velocity near the wall. This means that it is not necessary to resolve the entire boundary layer.

The conservation of mass is stated through the continuity equation:

$$\frac{\partial \rho}{\partial t} + \nabla \cdot (\rho \boldsymbol{v}) = 0 \tag{3-46}$$

Where
ρ = fluid density
$\boldsymbol{v}$ = fluid velocity vector

The momentum equations:

$$\frac{\partial(\rho \boldsymbol{v})}{\partial t} + \nabla \cdot (\rho \boldsymbol{v} \otimes \boldsymbol{v}) = -\nabla p + \nabla \cdot \tau + \boldsymbol{S}_m \tag{3-47}$$

where

$\otimes$ is a mathematical operator for the outer product of two vectors

τ = stress tensor

$\boldsymbol{S}_m$= momentum source

The stress tensor is linked to the strain rate through:

$$\tau = \mu\left(\nabla \boldsymbol{v} + (\nabla \boldsymbol{v})^{\boldsymbol{T}} - \frac{\mathbf{2}}{\mathbf{3}}\delta \nabla \cdot \boldsymbol{v}\right) \tag{3-48}$$

Where

μ = dynamic viscosity

δ = Kronecker Delta function

3.8.2 y^+ value

One of the critical parameters when performing CFD analyses is the y^+ value. It is a non-dimensional measure of the distance between the wall and the first node of a mesh, and gives an indication of how well the boundary layer is resolved [37]. The y^+ value can be calculated using (3-49)

$$y^+ = \frac{\Delta y \cdot u_\tau}{\nu} \tag{3-49}$$

Where u_τ is the friction velocity, Δy the distance to the first node from the wall and ν the kinematic viscosity. The y^+ value requirements depend on the turbulence model used. If the viscous sublayer is to be resolved very small distances are needed and the y^+ value required will be very small. On the other hand, wall functions that assume a logarithmic profile for the transitional boundary layer require higher y^+ values. When using wall functions a y^+ value of around 30-300 is recommended [41].

3.8.3 Damping calculations

CFX has a built-in method of computing the aerodynamic damping during flutter analyses. The damping is calculated as the work per vibration cycle done by the structure on the fluid. This means positive values indicates that the guide vane does work on the flow, which reduces the mechanical energy of the vibration. Thus, positive values mean that the vibration is damped. The work done by the structure is computed according to equation (3-50). It is important to note that the output is the work done over a cycle, not the damping ratio.

$$W_{cycle} = \int_{t_0}^{t_0+T} \int_{A} p\vec{v} \cdot \hat{n} \, dA \, dt \tag{3-50}$$

Where:
t_0= time at the start of the vibration
T = period of one cycle
p = fluid pressure
$\vec{v}$ = velocity of the blade
$\hat{n}$ = surface normal unit vector
A = blade surface area
The damping is then calculated using normalization as follows:

$$\zeta = \frac{W_{cycle}}{2\pi m \Omega^2 q_0^2} \tag{3-51}$$

where the denominator is the normalization. m is the mass, and is set to 1 kg as the modal solution is already mass normalized. Ω is the angular frequency of the motion in rad/s, while q_0 is a scaling factor that relates the modal amplitude and the imposed amplitude of motion:

$$q_0 = \frac{B_{imposed}}{B_{modal}} \tag{3-52}$$

4. The turbine

The turbine used in this case study is a high-head Francis turbine operating at 333.33 rpm. The turbine is typical for high-head operations in Norway and has a configuration of 30 runner vanes and 24 guide vanes. Some of the turbine parameters are listed in Table 1.

As the geometry of the turbine is the intellectual property of Rainpower, no detailed drawings or illustrations of the runner or guide vane have been used in the thesis. Certain illustrative plots will be presented using an old geometry. It is noted when different geometries are used for such illustrations.

Table 1: Turbine data

Head [m]	Specific speed [RPM]	Blade passing frequency, f_{gv} [Hz]	Guide vane frequency, f_b [Hz]
>500	333.33	166.67	133.3

The different parts of the guide vane will be referred to throughout the thesis using the names shown in Figure 12. The shaft has a diameter of 0.11 m and a total length of about 1900 mm.

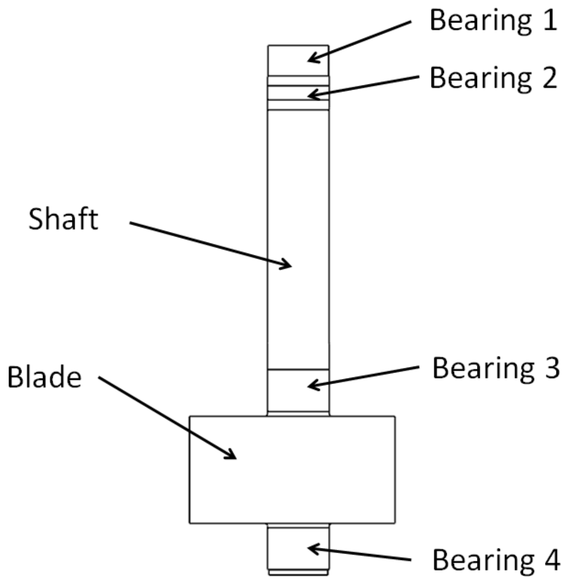

Figure 12: Names of the guide vane parts used in the thesis

5. Structural analyses

Several analyses are performed in order to evaluate the dynamic response of the guide vane. To understand the vibrational characteristics of the structure a modal analysis is performed. This outputs the mode shapes and corresponding frequencies of the structure, and forms the basis of a harmonic response analysis. The harmonic response analysis is used to evaluate the response of the guide vane responds to the dynamic pressure induced by rotor-stator interactions. The results will then be compared with those of a static structural analysis. The work flow is visualized in Figure 13.

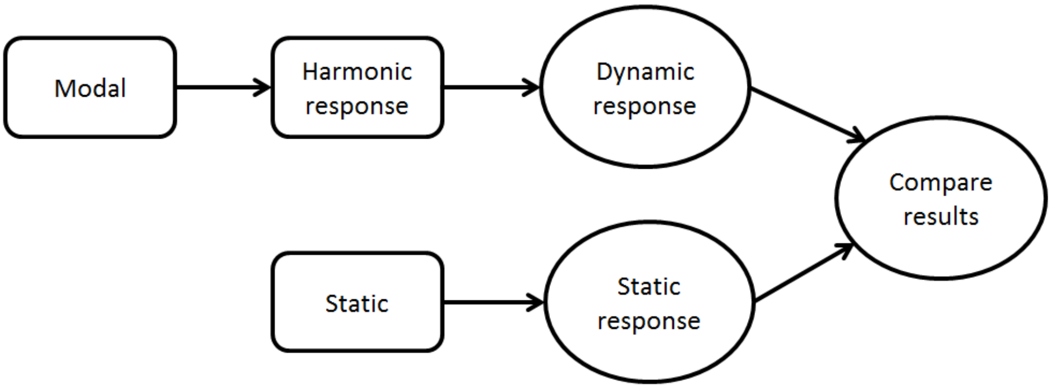

Figure 13: Work flow to evaluate the dynamic response

5.1 General settings

The following data and settings are used throughout the structural analyses in this project. Settings that are specific for each analysis are presented in the respective chapters.

5.1.1 Material data

Material	Density [kg/m^3]	Young's modulus (GPa)[2]	Poisson's ratio
Structural steel	7850	200	0.3

Material	Density [kg/m^3]	Speed of sound [m/s]
Water	997	1480

---

[2] This is the standard value for structural steel in ANSYS. The Young's modulus is often set to 210 GPa, however the actual value typically varies between 190-210 GPa. Using 200 instead og 210 GPa produces slightly higher deflections.

5.1.2 Acoustics

Acoustic elements are used to model the water in the structural analyses. Fluid viscosity is ignored for all of these analyses, meaning that friction is neglected. Thus, the analysis is undamped and only the added mass effect is evaluated. This assumption may lead to wrong mode shapes and natural frequencies. Simulations performed on a pump-turbine impeller performed by Egusquiza et.al [42] showed good correlation between the numerical and experimental mode shapes of a runner when friction was ignored. The differences in corresponding frequencies were within 2%. However, the runner and guide vane are inherently different geometries and results are not necessarily transferrable. As the damping in the system is not known, the alternative would be assuming a damping ratio. This would also be a potential source of error. It is therefore decided to perform the analyses without damping.

The fluid region is modeled by constructing a solid body that surrounds the guide vane blade. This domain is then assigned as an acoustic body, a feature available through the ANSYS ACT Acoustics extension. The surfaces of the fluid body are considered reflective. This makes it important that the acoustic domain representing the water is large enough that pressure waves do not cause interference when they are reflected. Meshing guidelines given in the ANSYS ACT Introduction to Acoustics lesson recommends at least 12 elements per wavelength [43]. The wavelength is computed as

$$\lambda = \frac{c}{f} = \frac{1\,450\; m/s}{166\; s^{-1}} = 8.7\; m \tag{5-1}$$

This is a very large number compared to the scale of the system. 12 elements across 8.7m would lead to very large elements. Any realistic mesh would easily fulfill this requirement. The acoustic domain used is shown in Figure 14 and the corresponding size presented in Table 2.

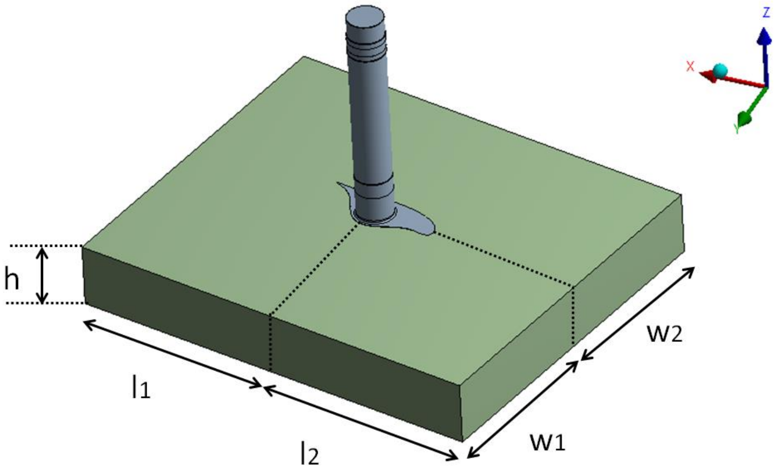

Figure 14: Acoustic domain size parameters

Table 2: Size of the acoustic domain

Parameter	Value [mm]
h	381
l_1	1193
l_2	1352
w_1	1122
w_2	1018

5.2 Modal analyses

5.2.1 *Modal analysis in air*

Setup

The first modal analysis is performed in air, and is useful to use for comparison when evaluating the added mass effect. This means that the acoustic domain is suppressed in this analysis. It is an undamped analysis for which the solver is set to “Program controlled”. The boundary conditions are shown on the left in Figure 15, where the purple colored face represents a fixed support and the red faces frictionless support. The mesh used is shown on the right in Figure 15, and the corresponding mesh data are listed in Table 3.

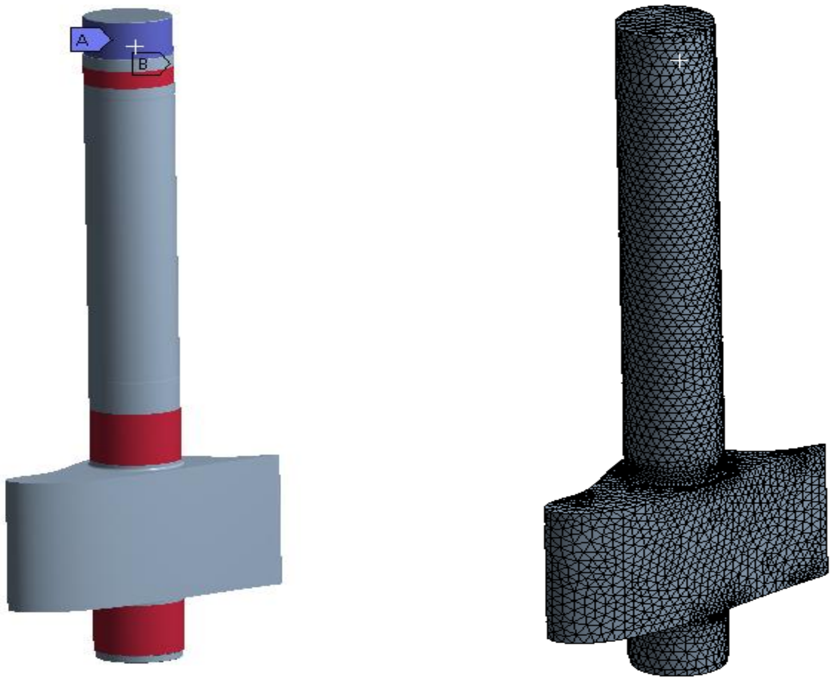

Figure 15: Guide vane boundary conditions (left) and mesh (right)

Table 3: Mesh information for modal in air analysis

Project	Size function	# of elements	# of nodes	Element type
Modal in air	Curvature	96 938	64 496	Solid187

Results

The natural frequencies of the first 6 modes are listed in Table 4. The first mode, shown in Figure 16, is the one of primary interest. It is the mode that is most likely to be excited and cause resonance, as the distance to resonance is only 4.7%. In this mode both the blade and shaft rotate back and forth around the center of the shaft. If excited, the largest deflections would be seen on the leading and trailing edges.

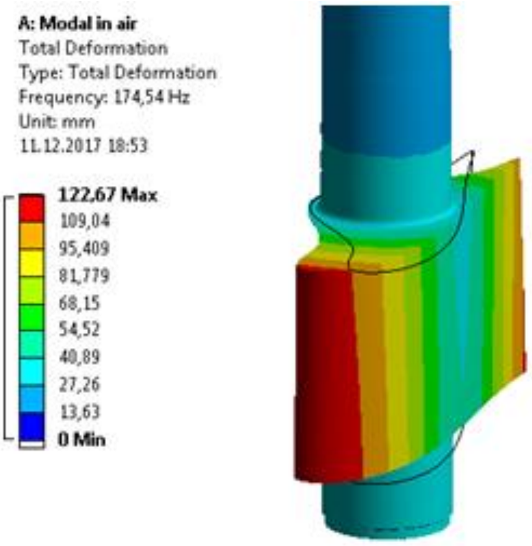
A: Modal in air
Total Deformation
Type: Total Deformation
Frequency: 174,54 Hz
Unit: mm
11.12.2017 18:53
122,67 Max
109,04
95,409
81,779
68,15
54,52
40,89
27,26
13,63
0 Min

Figure 16: Mode shape of the first mode in air

Table 4: First 6 natural frequencies of guide vane in air

Mode	Frequency
1	174.5
2	568.5
3	708.5
4	710.7
5	1059.5
6	1110.8

5.2.2 Modal analysis in water

Setup

To account for FSI effects it is necessary that nodes are shared on the fluid-structure interface. This ensures that the displacements are the same on the structure and fluid side. To achieve this, the geometry is generated using shared topology which creates a multibody part. The resulting mesh can be seen in Figure 17, and the mesh information is given in Table 5. The supports applied are the same as those for the analysis in air (shown in Figure 15).

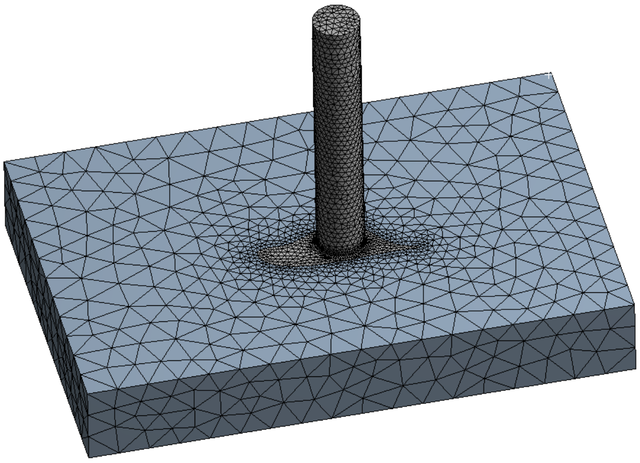

Figure 17: Modal acoustics mesh

Table 5: Modal acoustics mesh information

Domain	Size function	# of elements	# of nodes	# of shared nodes	Element type
Total	Curvature	96 847	137 813	7 596	
Guide vane		48 980	74 372		Solid187
Water		47 867	71 037		Fluid221

Results

A mesh optimization study is performed to ensure convergence of the solution and to determine the optimal mesh settings to avoid excessive calculation times. The mesh optimization study is performed with respect to the natural frequency of the first mode shape, and the result is shown graphically in Figure 18. Table 6 lists the first 6 natural frequencies of the system.

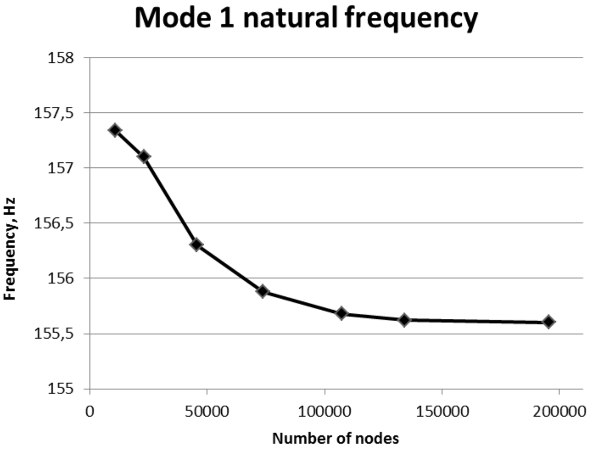

Figure 18: Mesh sensitivity analysis for the natural frequency of the first mode

Table 6: Natural frequencies of the first 6 modes

Mode	1	2	3	4	5	6
Natural frequency	155.7	285.2	314.2	450.4	561.3	586.3

Mode 1 corresponds to the same mode as for the analysis in air shown in Figure 16. The natural frequency of this mode is reduced from 174.5 Hz to 155.7 Hz, an 11% reduction. It is this mode that is of primary interest as the distance to resonance is only 6.5%. Mode 5 of the acoustic analysis corresponds to mode 2 in air, with a reduction of only 1%. However, this mode is mainly axial displacement which would be hindered by the turbine covers. None of the other modes in air and water matched when comparing the first 6 modes. It should be noted that the computed natural frequencies of some of the modes change substantially as the size of the acoustic domain is changed. However these modes are not of particular interest and focus is only given to the first mode.

5.3 Harmonic response analysis

Setup

A harmonic response analysis is performed to evaluate the stress and displacement amplitudes for the guide vane. This type of analysis requires a harmonic load. The load used in this project is provided by Rainpower in a .csv file which includes static and dynamic pressure data. These data were extracted at specified frequencies during a transient CFX analysis, and the pressure data contains real and imaginary components. As the turbine operates at fixed speed only a few frequencies may cause resonance. When considering the stator (guide vane) response, only integers of the blade passing frequency are of interest. According to Rainpower's experience the fundamental frequency is the frequency that typically matches the natural frequency of the structure. This corresponds to 166 Hz as listed in Table 1. Pressure data at 166 Hz is mapped onto the guide vane blade using external data in ANSYS Workbench, and the resulting imported pressure is shown in Figure 19.

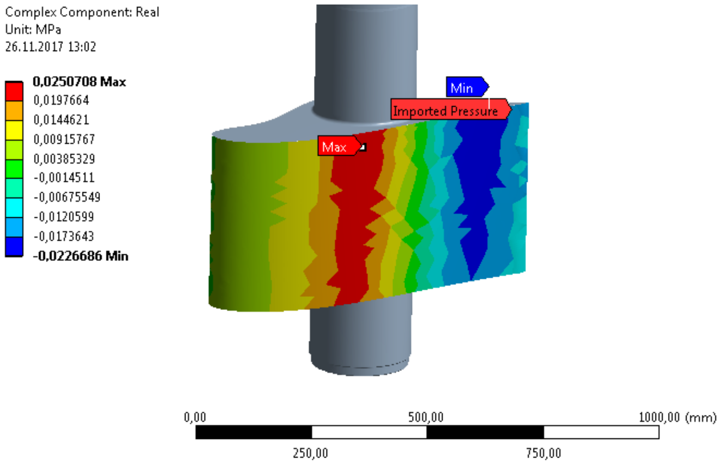
Complex Component: Real
Unit: MPa
26.11.2017 13:02
0,0250708 Max
0,0197664
0,0144621
0,00915767
0,00385329
-0,0014511
-0,00675549
-0,0120599
-0,0173643
-0,0226686 Min
Min
Imported Pressure
Max
0,00
500,00
1000,00 (mm)
250,00
750,00

Figure 19: Imported pressure for harmonic response analysis

As for the modal analysis with acoustic elements, shared topology is used to ensure a matching mesh at the fluid-structure interface. Different mesh settings are applied to better resolve areas of high stress. A mesh sensitivity analysis was performed, evaluating the torque and deformation amplitude. The results are shown in Figure 20, and the mesh statistics are shown in Table 7. Similar supports as in Figure 15 were applied with frictionless contact above and below the blade.

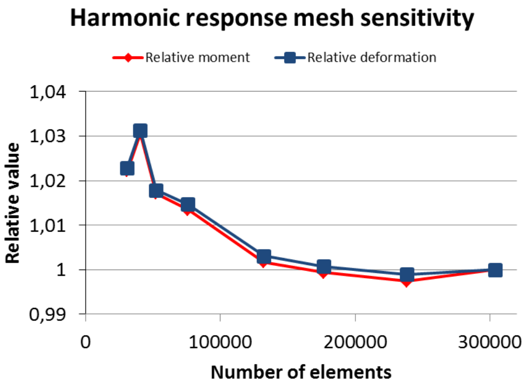

Figure 20: Mesh sensitivity of harmonic response analysis

Table 7: Mesh statistics for the harmonic response analysis

Domain	Size function	# of elements	# of nodes	# of shared nodes	Element type
Total	Curvature	91 303	132 260	3 976	
Guide vane		69 769	103 251		Solid187
Water		21 534	32 985		Fluid221

Important settings when performing a harmonic response analysis include the frequency range and number of solution intervals. These are controlled in the Analysis Settings. It is important to choose a frequency range that includes all modes that could be excited during operation. ANSYS calculates the response only at the frequencies determined by the intervals in the frequency range, and interpolates the results between these. Thus, in order to properly evaluate the response at normal operation it is important that the blade passing frequency is one of the frequencies ANSYS calculates at. During normal operation the turbine is fixed speed and runs at 333.33 rpm. Therefore the argument could be made that evaluating the response at the corresponding blade passing frequency alone would be sufficient. Still, the decision is made to perform the harmonic response analysis over a wider frequency range in order to properly visualize the excitation of modes and the distance to resonance. The frequency settings are listed in Table 8.

Table 8: Harmonic response analysis frequency settings

Frequency spacing	Range minimum	Range maximum	Solution intervals
Linear	86	686	120

As mentioned, the pressure data at 166 Hz. were extracted from a transient analysis and stored in a .csv file. These data only represent the actual pressure at 166 Hz; different frequencies would give different pressure data. This produces an error for all frequencies other than 166 Hz. If the specific response at other frequencies is of interest, pressure data extracted at these frequencies should be applied instead.

Results

The response spectrum of the stress amplitude is shown in Figure 21. The frequency response does not combine the results in different directions, thus the value of the reported stresses are not very meaningful. The plot is however useful to identify at what frequencies the peak values occur. As expected, the torsional mode peaks at around 155 Hz. Several peaks also appear in the region of 550 – 620 Hz. As the analysis is performed without damping the amplitude would reach infinity if a calculation point exactly corresponds with a natural frequency.

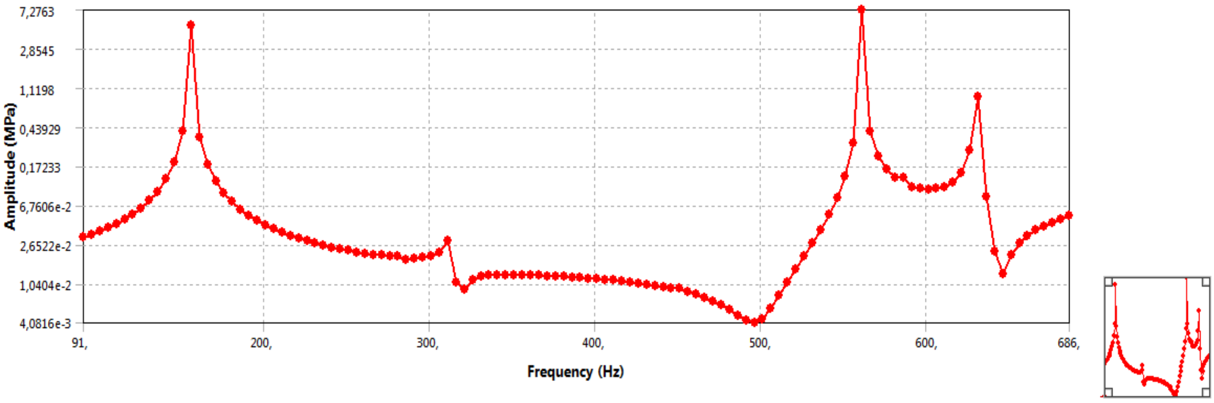

Figure 21: Harmonic response analysis stress amplitude spectrum

As noted it is the blade passing frequency at 166 Hz that is the frequency of interest. The maximum principal stress at this frequency is 11.3 MPa and seen on the radius that connects the blade and the shaft. The stress amplitudes are plotted in Figure 22.

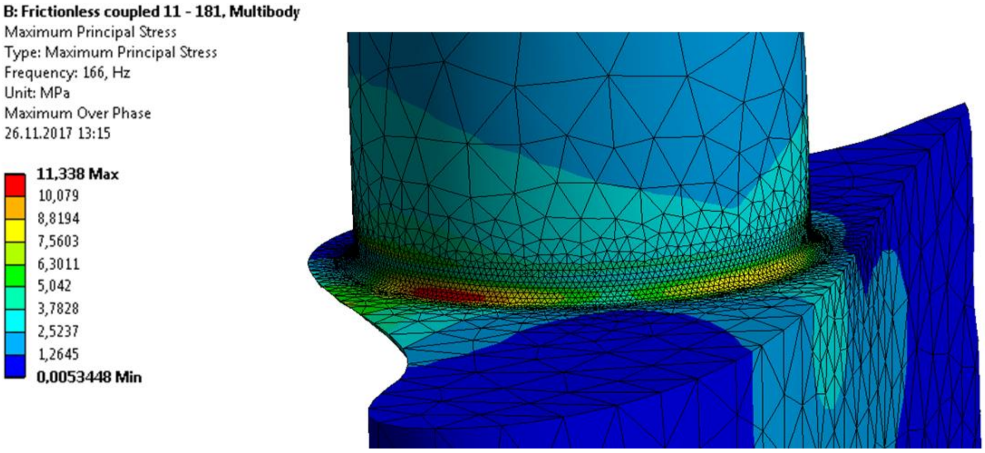
B: Frictionless coupled 11 - 181, Multibody
Maximum Principal Stress
Type: Maximum Principal Stress
Frequency: 166, Hz
Unit: MPa
Maximum Over Phase
26.11.2017 13:15
11,338 Max
10,079
8,8194
7,5603
6,3011
5,042
3,7828
2,5237
1,2645
0,0053448 Min

Figure 22: Plot of maximum principal stress amplitude

The maximum deformation of the guide vane at 166 Hz is 0.14 mm. This deflection is seen on the leading edge of the guide vane, shown in Figure 23 below. When comparing the deformed shape to the mode shape in Figure 16 it is clear that this mode is excited by the rotor-stator interactions.

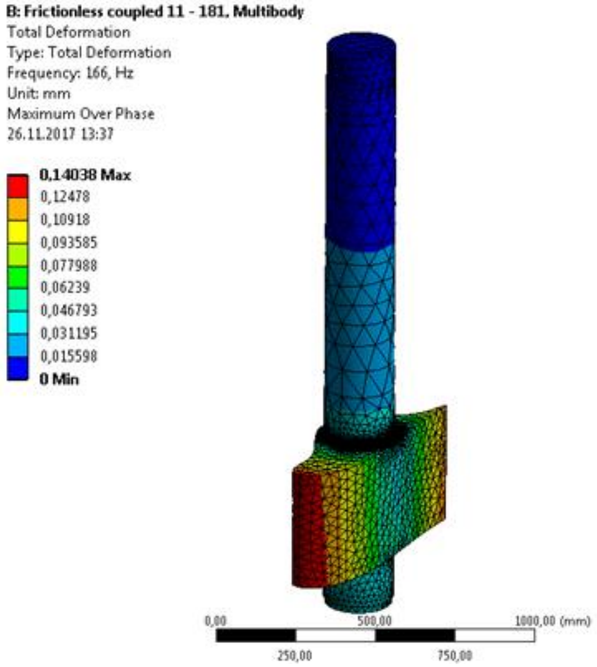
B: Frictionless coupled 11 - 181, Multibody
Total Deformation
Type: Total Deformation
Frequency: 166, Hz
Unit: mm
Maximum Over Phase
26.11.2017 13:37
0,14038 Max
0,12478
0,10918
0,093585
0,077988
0,06239
0,046793
0,031195
0,015598
0 Min
0,00
500,00
1000,00 (mm)
250,00
750,00

Figure 23: Deformation plot at 166 Hz

The harmonic response analysis outputs a dynamic moment of 4 616 Nm in the fixed support. It is this moment that causes the guide vane to vibrate. However this is based on the assumption of frictionless contact in the bearings above and below the blade. A static analysis is performed to evaluate the friction moment in these bearings. This is done in order to evaluate whether the assumption of frictionless contact is acceptable.

5.4 Static structural

A static analysis is required to evaluate the static force reactions in the guide vane bearings. The purpose of this is to evaluate the friction in these bearings to assess whether the frictionless assumption is applicable.

Setup

As for the harmonic response analysis, the external load for the static structural analysis is imported from a previous transient CFX calculation. The static structural analysis is performed using the same acoustic body as the harmonic response analysis. However, to improve the pressure mapping on the leading edge, a refined mesh is used that better resolves the curvature on the guide vane blade. Mesh data are given in Table 9 and the resulting mapping shown in Figure 24.

Table 9: Mesh statistics for the static structural analysis

Domain	Size function	# of elements	# of nodes	# of shared nodes	Element type
Total	Curvature	124 285	177 213	8 247	Solid187
Guide vane		83 636	124 271		Fluid221
Water		40 649	61 189		

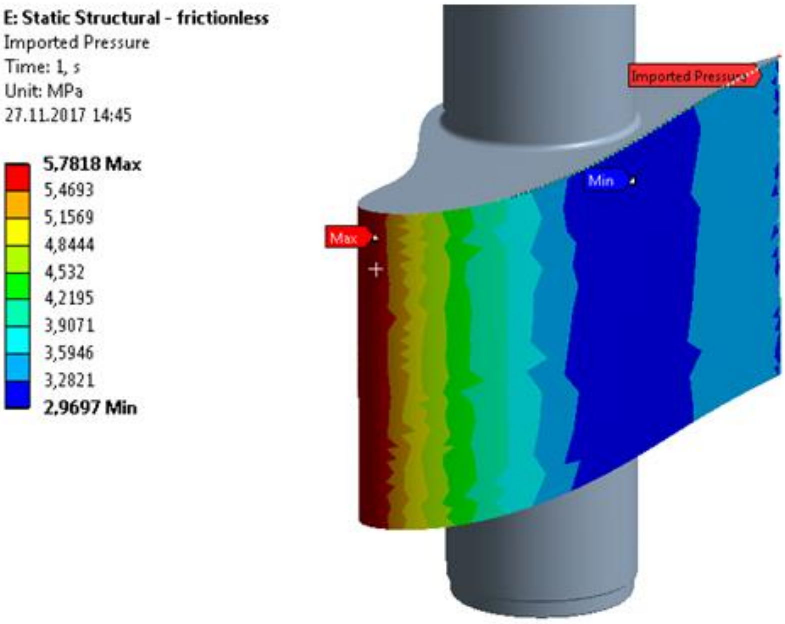

Figure 24: Mapped static pressure

Results

The resulting forces from the static load are reported as force bearing 1-4, numbered from top to bottom. Thus, the fixed support is bearing 1 and the bearings above and below the blade are number 3 and 4 respectively. The bearing forces are of interest to evaluate the static friction moment. Therefore the reported force is the resulting radial force in the bearing, computed as:

$$F_{bearing} = \sqrt{F_x^2 + F_y^2} \tag{5-2}$$

The results of the static structural analysis are shown in Table 10.

Table 10: Results from static structural analysis

Von Mises stress [MPa]	Deformation [mm]	Radial force bearing 1 [N]	Radial force bearing 2 [N]	Radial force bearing 3 [N]	Radial force bearing 4 [N]
42.9	0.30	1 550	3 240	234 800	233 400

Comparison with dynamic analysis

The radial bearing forces create a friction moment that counters the dynamic moment. Thus, if the friction moment is large compared to the dynamic moment, the assuming frictionless contact is not a good representation of the physical behavior of the guide vane. The following formula is used to compute the friction moment:

$$M_{friction} = F_{bearing} \cdot \mu_{fr} \cdot r \tag{5-3}$$

where F is the radial force, μ_{fr} the friction coefficient and r the radius of the guide vane shaft. An empirical value of 0.1 is used for the friction after discussion with turbine designer Petter Østby of Rainpower. The guide vane shaft diameter is 0.22m, which gives a radius of 0.11m. Friction moments from bearing one and two are neglected as the radial force in these bearings is much smaller than that of bearing three and four.

Table 11: Computed friction moment based on static bearing forces

Bearing	Radial force [N]	Friction force [N]	Friction moment [Nm]
3	234 800	23 480	2 580
4	233 400	23 340	2 570
Sum			5 150

The total friction moment in bearings 3 and 4 is 5 150 Nm. This is slightly higher than the reported dynamic moment of 4 616 Nm from the harmonic analysis. This indicates that the assumption of frictionless contact in bearing 3 and 4 is a bad approximation. The dynamic moment is not large enough to overcome the friction moment even at its maximum value. Considering that the dynamic moment is assumed to vary harmonically it is well below its maximum value at most points of the oscillation. According to these results the guide vane will not be allowed to slide in the bearing and fixed support would be a better approximation of the actual behavior. To analyze the effects of using fixed support a new modal analysis is performed.

5.5 Modal analysis with fixed support

As discussed the assumption of frictionless contact in the bearings above and below the blade is not appropriate. A modal analysis with fixed support in these bearings is performed to get a more realistic representation of the system. Apart from changing the supports to fixed, this analysis uses the same settings and mesh as the previous “modal analysis in water” (chapter 5.2.2).

5.5.1 *Results*

The first 6 natural frequencies of the system with fixed support are listed in Table 12. When compared to the previous modal analysis in water, the mode numbers from the frictionless support are used for reference. The following results are observed:

The torsion mode from the frictionless analysis completely disappears within the specified spectrum. This mode would now only include the blade as the shaft is fixed. Thus, the mode of primary interest is no longer close to resonance.

Mode 2 is now the lowest mode, but the frequency is not changed by the fixed support. Upon review it is clear that this mode is mainly dominated by deflection in the blade, and similar results are as expected. The same is true for mode 3 and mode 4. Mode 5 disappears of the same reason as mode 1, while mode 6 stays relatively unchanged

Table 12: Natural frequencies of the first 6 modes for analysis with fixed support

Mode	1	2	3	4	5	6
Natural frequency	285.2	314.1	450	586	631.3	696.7

5.6 Structural analyses conclusions

The results from the structural analyses give important insight when evaluating the dynamic response of the guide vane. As expected the natural frequency of the guide vane was close to resonance when frictionless support was used. This is the traditional method used by Rainpower when performing design analyses. However no resonance related issues have been observed for the guide vanes. The numerical structural analyses show that the combined friction moment in the bearings above and below the blade is larger than the torque exerted by the rotor-stator interactions. This leads to the conclusion that the frictionless contact assumption is not a good representation of the system. When using fixed support instead the stiffness of the system is completely changed. The torsion mode expected to cause resonance no longer appears in the modal analyses. For the case studied the conclusion is that resonance problems are most likely not seen because the bearing friction is so large that the shaft does not move.

6. CFX analyses

The purpose of the CFX analyses is to investigate the hydrodynamic damping for the guide vane exposed to RSI. As shown in chapter 5 the bearing friction causes the guide vane to be fixed in the bearings. However, this may not be true for all turbines. Therefore it is of interest to evaluate what hydrodynamic damping may be expected if the torsion of the guide vane is not restricted by friction. For simplicity, when the term damping is used in this chapter, it refers solely to hydrodynamic damping.

A number of assumptions are made when performing the CFD analyses that follow:

- Frictionless contact in the bearings, as modelled in chapter 5.2.2
- The torsion mode shape derived from chapter 5.2.2 is representative of the guide vane motion
- Damping is frequency independent
- Flow is completely symmetric around the turbine

6.1 General settings

Because the turbine is assumed to be perfectly symmetric and there are 24 guide vanes, only a sector that spans 360/24 = 15 degrees is considered. The fluid domain is constructed as a section of a hollow cylinder with an inner diameter of 2100 mm and an outer diameter of 3000 mm. If a cylindrical pattern is applied the 24 sectors span a full 360 degrees, as shown in Figure 25.

The CFX calculations are based on the peak load flow. At peak load the guide vane opening angle is 12 degrees. This means that each guide vane is rotated 12 degrees from the point where they interlock, visualized using an old guide vane profile in Figure 26. Flow is assumed to enter from the outer surface at a rate that corresponds to full load. The inflow angle χ is 25 degrees, defined as:

$$\chi = tan^{-1}\left(\frac{v_{rad}}{v_{tan}}\right) \tag{6-1}$$

Where v_{rad} is the radial and v_{tan} the tangential component of the velocity. The ratio $v_{rad}\,/v_{tan}$ is 0.4663. It follows that the radial velocity component is 0.318 and the tangential component 0.682.

The same material data for water as for the structural analyses are applied; however viscosity must be accounted for in the damping calculations.

Material	Density [kg/m^3]	Speed of sound [m/s]	Viscosity [kg/m·s]
Water	997	1480	0.00089

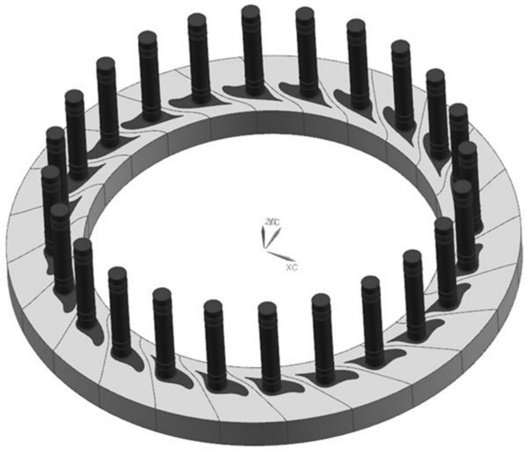

Figure 25: Visualization of guide vanes around the turbine

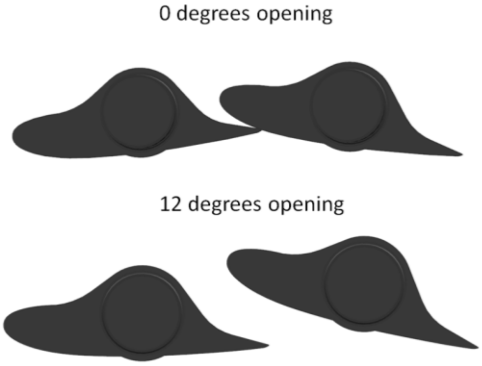
0 degrees opening
12 degrees opening

Figure 26: Guide vane opening angle

When performing the analyses the guide vane itself is suppressed. This leaves a cavity shaped as the guide vane blade, shown in green in Figure 27. The faces of this cavity are assigned “no slip wall” boundary type along with the upper and lower face of the fluid domain. The inlet flow is specified with radial and tangential velocity component, while the relative outlet pressure is set to 0 atm. Note that the arrows that indicate the inlet face are normal to the surface and do not represent the direction of flow. Rotational periodicity is defined on the sides of the fluid domain. This setting ensures that these faces are not treated as walls but instead as extensions of the domain. Flow “leaving” the domain on one side would be replaced by flow entering the domain on the opposite side. This is computationally much simpler than modelling the whole 360 degree span.

The SST turbulence model is applied in the CFX analyses. The SST turbulence model uses automatic wall treatment which automatically switches wall functions on and off depending on how well the boundary layer is resolved (the y^+ value).

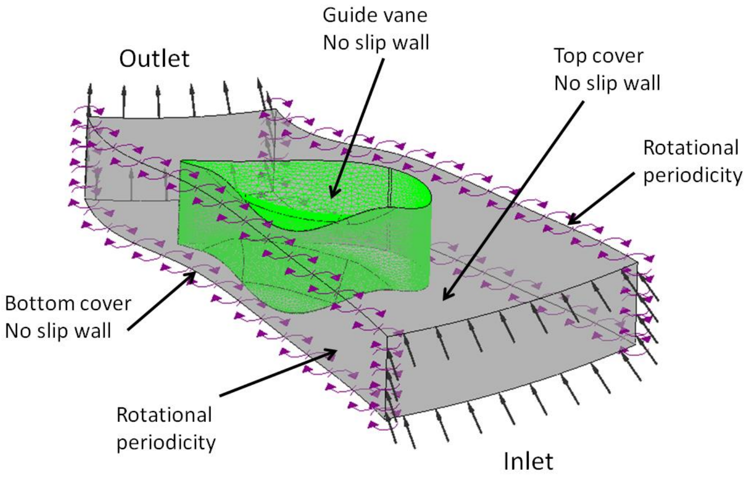
Guide vane
No slip wall
Outlet
Top cover
No slip wall
Rotational
periodicity
Bottom cover
No slip wall
Rotational
periodicity
Inlet

Figure 27: CFX boundary conditions

6.2 Steady state analysis

The purpose of the steady state analyses is to evaluate different mesh settings and find a proper mesh for the transient analyses. The steady state analyses are much faster than the transient ones. Thereby a lot of time can be saved performing the mesh sensitivity analyses on the steady state tests.

No motion is applied to the guide vane boundary in the steady state tests. To analyze for mesh convergence the pressure loss between the inlet and outlet face is chosen as the analysis parameter. The mass averaged pressure is chosen to account for total pressure. The mass averaging in CFX is based on the following equation:

$$massFlowAve(\phi) = \frac{\sum(m\phi)}{\sum m} \tag{6-2}$$

Where ϕ is the parameter being averaged, in this case pressure, and m the local mass flow. Both the mass flow and pressure are evaluated at each node of the 2D surface chosen. The results of the mesh convergence tests are shown in Figure 28. All meshes were performed with a cyclic symmetry region to ensure matching meshes at the rotational periodicity sides of the fluid body.

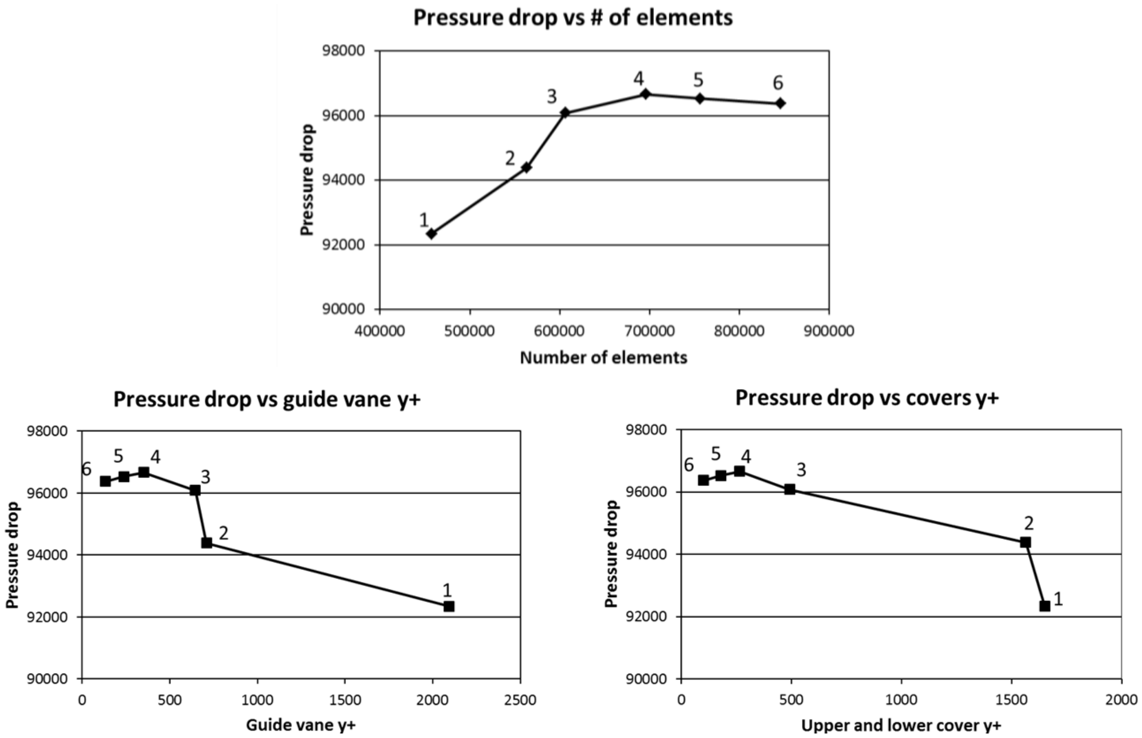

Figure 28: Mesh convergence plots for steady state analysis

Table 13: General mesh settings used in CFX analyses

Size function	Relevance center	Max face size	Transition	Span angle center	Min size	Max tet size	Curv. angle
Curvature	Coarse	20	Slow	Fine	5	40	0.05

Table 14: Number of inflation layers around guide vane profile and covers

Mesh	1	2	3	4	5	6
# of elements	457 238	563 161	606 536	696 228	756 435	846 013
# of nodes	138 057	189 406	213 934	259 488	289 951	335 466
# of guide vane inflation layers	5	10	10	13	15	18
# of cover inflation layers	5	5	10	13	15	18

The largest changes in pressure drop are seen between mesh 1, 2 and 3. For mesh 2 the guide vane y^+ value has changed to around 650, which has a clear effect on the pressure drop. The same is seen for the change from mesh 2 to 3, when the cover y^+ values are lowered to around 500. Further increasing the number of inflation layers lowers the y^+ value below the upper limit of the recommended range of 30-300. However only small changes in pressure drop are seen between mesh 3 - 6. The following transient analyses will be performed using two of the meshes above: Mesh 3 and mesh 5. This is done to assess if there is any change in results for y^+ values above and below 300. The mesh quality statistics for these meshes are given in Table 15. The element qualities are calculated by CFX when the analysis is initiated. There are three qualities: ! means the quality is questionable, ok is acceptable and OK is good. It is seen from the values that the majority of elements are of good quality, and that very few elements are questionable.

Table 15: Mesh quality statistics

Mesh	Orthogonal angle			Exponential factor			Aspect ratio		
	% !	% ok	% OK	% !	% ok	% OK	% !	% ok	% OK
3	<1	5	95	<1	4	96	0	0	100
5	<1	1	99	<1	1	99	0	<1	100

6.3 Transient analyses

6.3.1 Setup

Transient analyses are required in order to evaluate the hydrodynamic damping of the guide vane. This implies that some motion must be assigned to the guide vane profile. By assuming that the RSI will excite the first mode found in the modal analysis in air (Figure 16), the motion of the guide vane can be represented by the mode shape and its corresponding natural frequency. The amplitude of this motion is found in the harmonic response analysis to be 0.14mm on the leading edge.

The guide vane profile is forced to vibrate in CFX by setting the mesh motion option to “periodic displacement”. The mode shape and natural frequency are extracted from the modal analysis and stored as normalized displacement coordinates in a .csv file. The normalization makes sure that the deflection in the point of maximum modal displacement is set to 1mm. All other points are scaled in proportion to this. The .csv data are then mapped onto the guide vane profile. By setting the amplitude of this motion to 0.14 mm a displacement scaling is performed, and all of the normalized displacements are scaled by 0.14/1.

Table 16: Boundary settings for guide vane profile

Motion profile	Mesh motion	Displacement type	Boundary condition	Frequency [Hz]	Amplitude [mm]
Mode 1 of modal analysis in air	Periodic displacement	Normalized Cartesian coordinates	No Slip Wall	155.7 Hz	0.14

The transient analyses type is set to “transient blade row”. This setting enables the user to model only one or two blades instead of the whole turbine. It is also sufficient to model only a few blade passages in order to gain relatively accurate results. Important settings for the blade row model include the transient blade row model, transient method, time period, timesteps and time duration. The time period is defined as 1/frequency, where the defined frequency is the natural frequency of the mode shape, 155.7 Hz.

Table 17: Transient blade row model settings

Blade row model	Transient method	Time period [s]	Number of periods per run
None	Time Integration	0.00642	5

Two methods to calculate the damping are applied, controlled in the “output control” section. The calculated damping should ideally be similar for these two methods:

- Pre-defined “aerodynamic damping” under the monitor tab, calculated as explained in chapter 3.8.3. Both a full period integration and a moving integration interval monitor are applied. If these two converge it is a sign that sufficient blade passings are modelled.
- Transient statistics logging of the arithmetic average value of wall work density. The logging begins on the first iteration of the last blade passing and reports the average value of wall work density over the last blade passing interval.

Both of these methods output the work done by the guide vane on the flow. The damping is computed according to equation (3-51). The modal amplitude found in the modal analysis is 122.57 mm, the imposed amplitude 0.14 mm and the frequency of motion 155.7 Hz. Thus the damping is calculated using the following normalization:

$$\zeta = \frac{W_{cycle}}{2\pi \cdot (2\pi \cdot 155{,}7)^2 \cdot \left(\frac{0{,}14}{122.57}\right)^2} = \frac{W_{cycle}}{7.83} \qquad (6\text{-}3)$$

An important settings parameter that needs to be investigated by testing is the number of timesteps per period. This defines how many points in the time domain CFX calculates for in each blade passing period.

6.3.2 Results

A number of timesteps per period settings are tested to ensure sufficient partition in the time domain. The different settings are tested both for mesh 3 and 5, and the effect on the monitor and wall work density damping is shown in Figure 29. The tested settings are 24, 48, 96, 144 and 192 (mesh 3 only) timesteps per period.

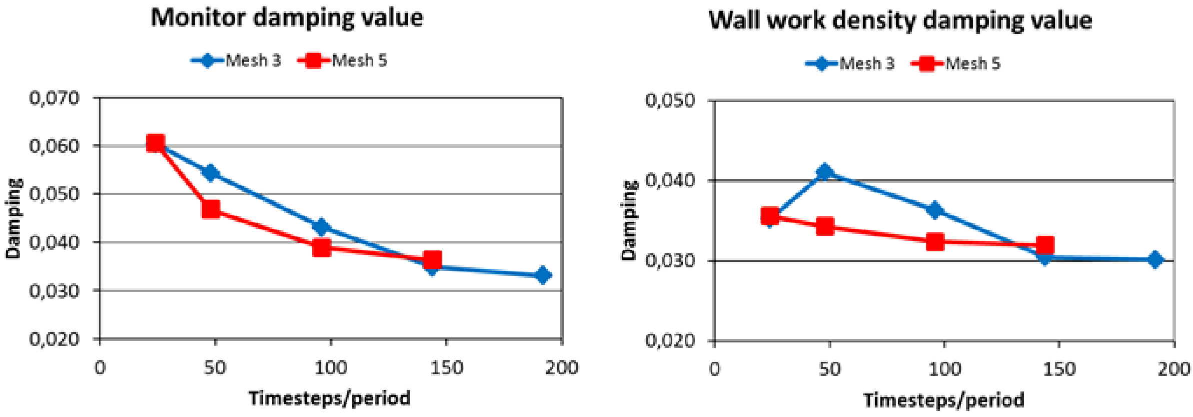

Figure 29: Plot of calculated damping for different timesteps.

Increasing the number of timesteps decreases the monitor damping for both meshes. At 24 timesteps the calculated damping is around 6% both for mesh 3 and 5. By increasing the number of timesteps for mesh 5 the monitor damping value seems to converge as the damping changes less and less for each timestep before it appears to stabilize at around 3.5%. The calculated damping for mesh 3 changes almost linearly between 24 and 144 timesteps/period. Less change is seen when the number of timesteps is increased to 192, and the curve appears to level out at around 3.2%.

The damping value calculated using wall work density is less affected by changing the number of timesteps per period. Again, the damping values found at 24 timesteps is the same for both meshes. For mesh 5 the damping value does not change much with increased number of calculation points. Going from 24 to 144 timesteps/period, the damping only changes from 3.5% to 3.1%. The damping found using mesh 3 shows no clear pattern, increasing at 48 timesteps then decreasing again as even more calculation points are used.

In order to properly evaluate the two different meshes, Figure 30 better shows the convergence of the damping values and difference between the two methods.

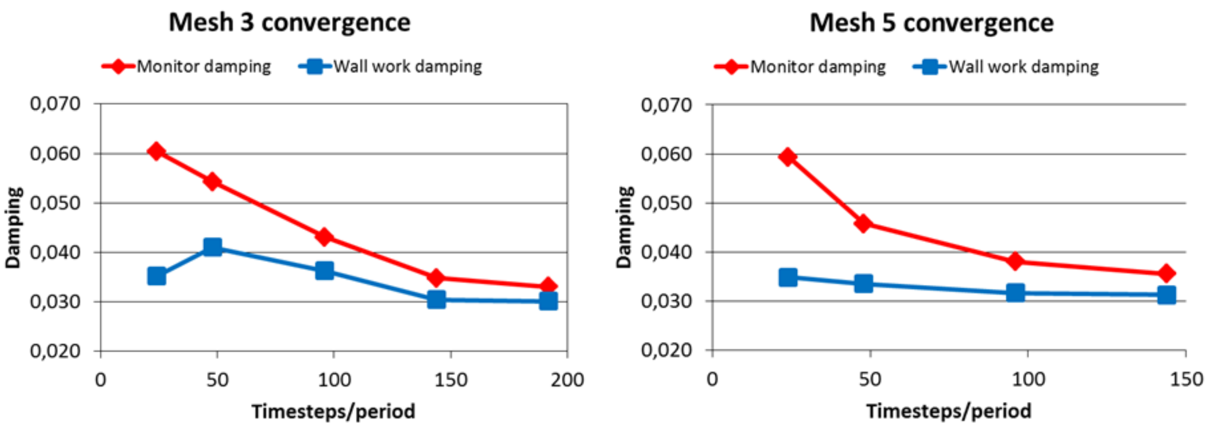

Figure 30: Comparison of damping from monitor and wall work density calculations

It is also important to take the solution time into consideration. The time for both meshes at different timestep settings are shown in Figure 31. The analyses take shorter time to finish when mesh 3 is used. At 24 timesteps per period the analyses take nearly twice as long. As the number of timesteps per period is increased to 96 the difference increased and the analysis took about twice as long using mesh 5. At 144 timesteps per period the difference is reduced.

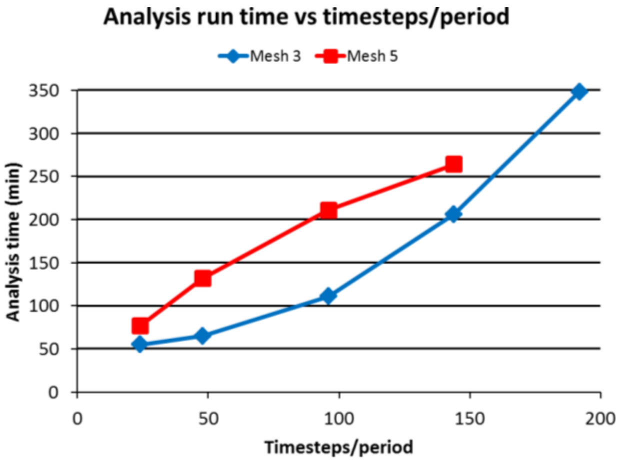

Figure 31: Plot of analysis run time versus number of timesteps per period

Based on these results, mesh 5 with 96 timesteps/period is chosen for the further analyses. The average y^+ value is 237 for the guide vane profile and 179 for the covers, both within the recommended range. The results for mesh 5 display a better convergence and more desirable characteristics when the number of timesteps is changed. The analysis took 3h31m.

A midplane velocity plot of the CFX results shows a clear stagnation point on the leading edge of the guide vane, a different velocity on the pressure and suction side, and wake effects on the trailing edge of the profile. Permission to show the plot was not given as it would show the guide vane profile. However, for visualization, the flow field around a different geometry is provided in Figure 32. The same phenomena are obtained by Thapa et al [24] in their experiments when applying particle image velocimetry to a guide vane geometry

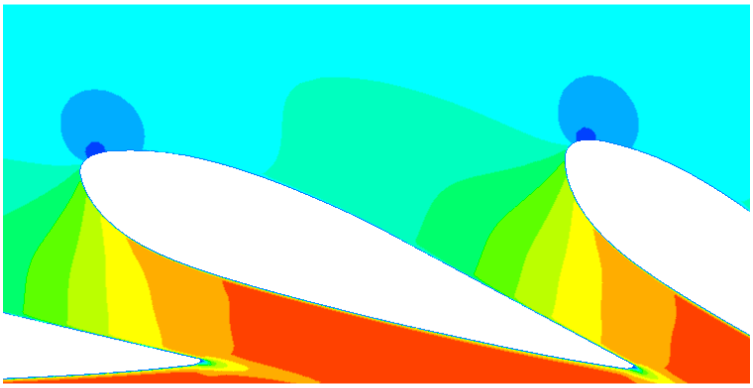

Figure 32: Velocity plot around guide vane profile. For visualization[3]

Review of the results

Figure 33 below shows the two aerodynamic damping monitors. The full period integration (red) and moving integration integral (green) both converge well. This indicates that sufficient blade passings are modelled. The argument could even be made that four passings instead of five could suffice as the change for the last period is very small. This would reduce the analysis time.

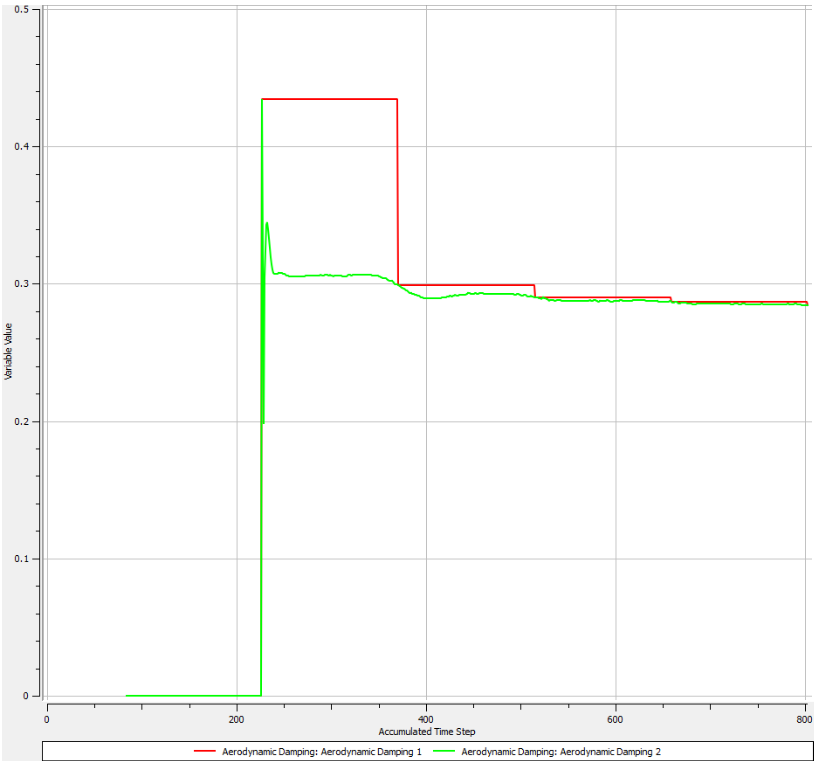

Figure 33: CFX aerodynamic damping monitors.
Red: Full period integration. Green: Moving integration interval

---

[3] The velocity plot is provided by Rainpower for visualization. It does not represent the results obtained in this thesis, nor is it the actual guide vane profile of the turbine.

Other indicators for convergence are the residuals of momentum and mass. The residuals give an indication to how accurately the governing equations are solved. Both the root mean square (rms) and maximum value of residuals may give insight to the convergence. The CFX modelling guide gives the following explanation of three rms residual levels:

- 1e-4 is considered loose convergence, and may be sufficient to obtain a quantitative understanding of the flow
- 1e-5 is good convergence and usually sufficient for most engineering applications
- 1e-6 or below is very tight convergence. Such low values are often unachievable, however it may be required for geometrically sensitive problems.

The rms residuals from the analysis are shown in Figure 34. All the rms-residuals stay below 1e-5, indicating that that good convergence is achieved. The max values (not shown) are much higher, ranging from 2e-3 to 1e-4. However, according to the CFX modelling guide this is not uncommon.

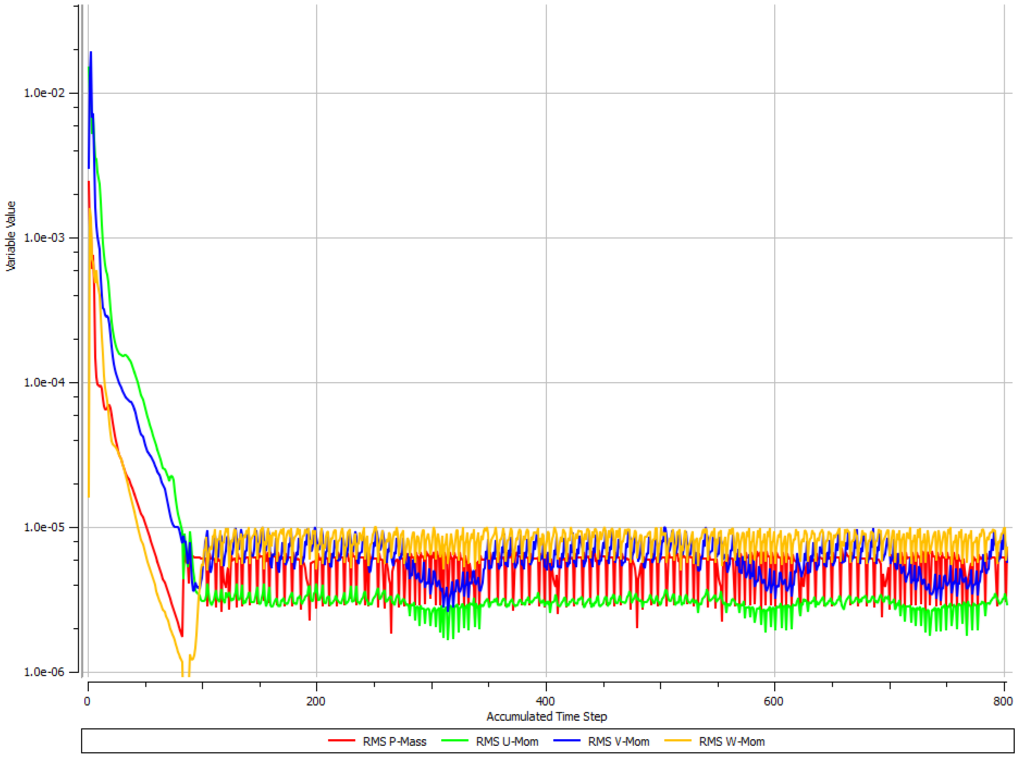

Figure 34: Rms residuals of CFX analysis with 144 timesteps per period and mesh 5

A plot of the averaged wall work density over the last period is shown in Figure 35. It appears that the leading edge does work on the fluid on the suction side and that the fluid does work on the guide vane on the pressure side. Moving along the profile on the pressure side the wall work density changes from negative to positive, indicating that the trailing edge also does work on the fluid. Relating to damping this means the leading edge pressure side is negatively damped (energy is added to the guide vane movement), while the leading edge suction side and trailing edge pressure side are damped (energy is removed from the motion). The damping value calculated is the area integral over of the wall work density on the guide vane surface.

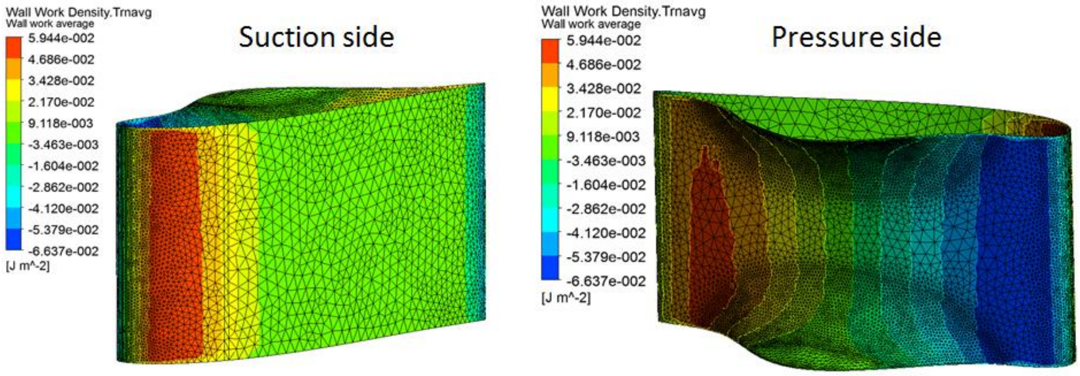
Wall Work Density.Trnavg
Wall work average
5.944e-002
4.686e-002
3.428e-002
2.170e-002
9.118e-003
-3.463e-003
-1.604e-002
-2.862e-002
-4.120e-002
-5.379e-002
-6.637e-002
[J m^-2]
Suction side
Wall Work Density.Trnavg
Wall work average
5.944e-002
4.686e-002
3.428e-002
2.170e-002
9.118e-003
-3.463e-003
-1.604e-002
-2.862e-002
-4.120e-002
-5.379e-002
-6.637e-002
[J m^-2]
Pressure side

Figure 35: Plot of wall work density averaged over the last period

6.3.3 Damping vs amplitude

Similar analyses are performed with different amplitudes in order to assess how the viscous damping is affected by the amplitude of motion. The analyses are performed using mesh 5 with 96 timesteps/period. The amplitudes tested, corresponding normalization and calculated damping are listed in Table 18. The analysis time was around 3h30m for all amplitudes tested.

Table 18: Results from damping versus amplitude study

Amplitude (mm)	0.05	0.14	0.2	0.3	0.6	0.1
Normalization	0.999	7.83	15.99	35.97	143.86	399.62
Monitor damping	0.389	0.0389	0.0389	0.0389	0.0388	0.0386
Wall work damping	0.0329	0.0324	0.0324	0.0324	0.0323	

The analyses show no significant change in damping ratio for the tested amplitudes. The monitor calculated damping is around 3.9% and the wall work damping 3.2% regardless of the amplitude.

6.4 CFX conclusions

The CFX analyses clearly show the importance of sufficient calculation points in the time domain. Although the analyses take longer to finish, more accurate results can be expected. This will always be a compromise when performing numerical analyses; how good results are required versus how long analysis time is acceptable. For the analysis performed using the amplitude found in the structural analyses, 0.14mm, the calculated damping is around 3-3.5% depending on the calculation method. The low rms residual values indicate with good confidence that convergence is achieved. This is further backed by the mesh sensitivity analysis performed for the steady state friction loss, and the convergence tests for number of timesteps. No significant change in the damping ratio was seen when different amplitudes were tested.

6.5 Damped vs undamped harmonic response analysis

A damped harmonic response analysis is performed to assess the effect of damping. The setup is the same as that in chapter 5.3, but damping controls are applied in this analysis. The damping is modelled as Rayleigh damping, which requires input of the damping coefficients α and β. By assuming that the sum of contributions from these terms is nearly constant over a frequency spectrum, these constants can be evaluated as:

$$\alpha = 2\zeta \frac{\omega_1 \omega_2}{\omega_1 + \omega_2} \tag{6-4}$$

$$\beta = \frac{2\zeta}{\omega_1 + \omega_2} \tag{6-5}$$

By using ζ= 0.035, ω_1= 155.7 Hz and ω_2= 170 Hz (arbitrarily chosen), the coefficients are:

- α = 5.6869
- β = 0.000215

Figure 36 shows the frequency response of the undamped (top) and damped (bottom) analysis over a frequency span of 140 – 170 Hz. The damping effect is clearly visible. The total deformation and maximum principal amplitudes of the two analyses are listed in Table 19

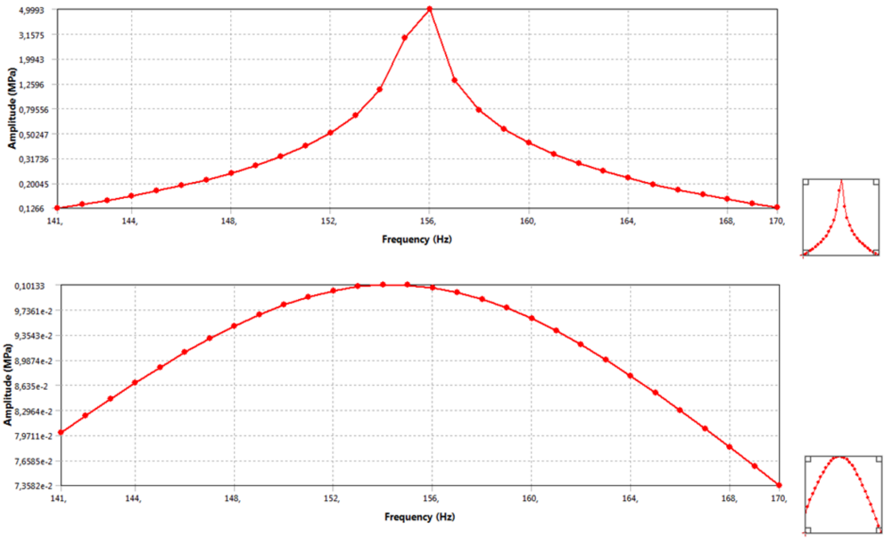

Figure 36: Frequency response of damped and undamped models

Table 19: Results from damped and undamped harmonic response analysis

Model	Maximum principal stress	Total deformation	Torque
Undamped	11.3 MPa	0.14 mm	4 616 Nm
Damped	5.76 MPa	0.072 mm	2 443 Nm

7. Discussion and conclusion

The discussion section is split into two parts. The first part is a general discussion where the aim is to highlight the applicability of the obtained results. While the results obtained appear conclusive for this exact turbine they should not automatically be assumed to be valid for all high-head turbines. The second part is focused on the numerical models applied.

7.1 General discussion

The work in this thesis is a case study of a single high-head Francis turbine. While the results show that the torque acting on the guide vane is not large enough to overcome friction in the bearings, it cannot automatically be assumed that this is the case for all turbines. For example, the size of the vaneless space between the guide vane and runner is a key parameter for the rotor-stator interaction [29]. For smaller radial gaps, the pressure increase and flow field distortion caused by the passing runner vanes are amplified. This would increase the torque on the guide vane. Another parameter that may change the results is the shape of the guide vane profile. As explained by Antonsen, the shape of the guide vane profile affects the pressure difference between the pressure and suction side of the guide vane [26]. A large part of the radial force that creates the friction moment in the bearings is a result of this pressure difference. He also states that the number of guide vanes and runner vanes does affect the severity of rotor-stator interactions. Thus, care must be taken if the results presented in this thesis are to be applied in turbine design.

When comparing the results of the harmonic response analyses with and without damping it is clear that the viscous damping does play a significant role. The amplitudes of maximum principal stress and deformation are about half of those found in the undamped model. The resulting torque in the bearing is almost half as well. This indicates that modelling the damping should be performed if detailed stress calculations are to be performed, for example in the case of fatigue life estimation. However it is hard to draw general conclusions to whether the damping alone would be enough to save the structure in case the bearing friction is not large enough to restrain the guide vane.

The analyses performed are restricted to calculations at full-load. Other phenomena than the rotor-stator interactions may dominate at part load such as flow separation or vortex shedding. However, turbines are designed to operate without significant flow separation when the load is around the best efficiency point. When comparing operation at full-load and at the best efficiency point however, the radial gap is less at full-load. As discussed the torque exerted by the RSI should therefore be lower at the best efficiency point.

No comparison with experiments has been performed. This makes it impossible to say how well the results coincide with the actual response of the guide vane. It would be virtually impossible to reproduce the exact flow conditions of the turbine in a laboratory. If experimental results were to be obtained, measurements would have to take place at the actual turbine. Measurements in the waterway would be hard to obtain, however assessing whether the guide vane overcomes friction in the bearings might be possible to measure, i.e. using accelerometers mounted on the shaft.

7.2 Notes on the numerical modelling

There will always be certain error in the results of numerical analyses. The objective of using numerical models is to achieve results that are sufficiently accurate for practical use. As noted it is hard to quantify the accuracy of the obtained results without any comparison to experimental results.

A number of factors affect the accuracy of the results. Both the structural and CFD analyses are mesh dependent. Mesh sensitivity analyses were performed to find mesh configurations that gave well converging results without excessive computational cost. The y^+ value is another important mesh parameter for the CFD analyses. This was also tested for convergence in the mesh sensitivity analyses. The average y^+ values are also within the recommended range of 30-300 when using wall functions. This gives reason to assume that the meshes are not a cause of significant error in the results.

The transient CFD analyses are performed as 1-way FSI. Periodic motion is applied to the guide vane profile, and CFX estimates how this affects the flow. There is no feedback in the system. This means that the flow does not affect the motion of the guide vane. Not accounting for this effect may produce errors in the results. However, when Zhu et al., compared the results of 1-way and 2-way FSI for a Francis turbine, the results were within 1% [44]. They argue that, for small deflections, 1-way and 2-way FSI produce similar results. Their results were based on maximum deflections of around 0.5 mm, around three times as large as the deflections studied in this thesis. As the geometries of runners and guide vanes are completely different the results are not necessarily the same when studying guide vanes.

The mode shapes and natural frequencies found in the modal analyses are performed without taking the nearby turbine parts into account. The size of the acoustic domain is larger than the distance between adjacent guide vanes. Pressure waves would reflect off these surfaces which might cause some change in the added mass effect. Modelling this, however, is not straightforward, but the effects are considered negligible. The modal analyses are also performed in for the guide vane submerged in non-flowing water. This is the conventional way to perform these analyses and is not considered a source of large error.

The analyses of torque and friction moment are based on either the assumption of frictionless or fixed support in the guide vane bearings. The actual friction can be represented as Coloumb friction. However, modelling Coloumb friction requires the use of non-linear terms. Modelling this type of friction cannot be done directly in a harmonic response analysis as this analysis type only handles linear terms. The actual response could be modelled using a transient analysis, which allows for non-linear terms. This could be useful in case the torque, which varies sinusoidally, overcomes the friction during parts of the oscillation.

When performing the CFX analyses, the model is constructed without gaps between the guide vane blade and the covers. These gaps are the cause of leakage flows, as explained by Chitrakar et al. [13]. Leakage flows may cause vortices, and reduces the effective pressure difference between the pressure and suction side. As this is not the scope of this thesis, these simplifications have been necessary in order to reduce the size of the computational domain.

Some problems were encountered when trying to use the results from the modal analysis in air to perform the CFX analyses. The modal displacements obtained led to a very strange normalization of the results. After discussions with Rainpower and representatives from EDR Medeso, it was decided to use the mode shape and natural frequency obtained in the modal analysis performed in air. Upon inspection it is clear that the mode shapes from the analyses in air and water are very similar, and it is assumed that using this mode shape is not a significant source of error. The author has not been able to find other papers that discuss the effect of added mass on the mode shape of a guide vane. However, studies of other geometries underbuild this assumption. Liang et al. showed that the mode shapes of a runner were virtually unchanged from air to water [5]. Similar results are found by Vu et al. for a vibrating plate [45].

7.3 Conclusion

A numerical study of fluid-structure interactions in a Francis turbine has been carried out. The main goal of the project has been to evaluate the dynamic response of the guide vanes to rotor-stator interactions in order to evaluate why resonance is not a common problem for this part of the turbine.

The resulting torque from RSI was computed using a harmonic response analysis. The result was then compared to the friction moment in the guide vane bearings from a static structural analysis. The results from these analyses indicate that the torque is not large enough to overcome friction. The corresponding modal analysis, where the guide vane is fixed in these bearings, shows that the natural frequency of the mode that was likely to cause resonance disappears from the specified frequency spectrum. This is likely the reason resonance has not caused problems in the guide vanes of this turbine.

Damping calculations were performed in an attempt to evaluate if the damping would be large enough to overcome resonance in case the friction is not large enough to restrict the guide vanes. The damping was found to be around 3.5% and independent of the amplitude of the motion. However, drawing general conclusions from the damping results was deemed hard as the project has not focused on stresses in the guide vane.

References

1. *International Energy Outlook*. 2016, U.S. Energy Information Administration https://www.eia.gov/outlooks/ieo/.
2. *Renewables Information: Overview*. 2017, International Energy Agency.
3. *REthinking Energy 2017: Accelerating the global energy transformation*. 2017, IRENA: Abu Dhabi.
4. Seidel, U., et al., *Evaluation of RSI-induced stresses in Francis runners.* IOP Conference Series: Earth and Environmental Science, 2012. **15**(5): p. 052010.
5. Liang, Q.W., et al., *Numerical simulation of fluid added mass effect on a francis turbine runner.* Computers & Fluids, 2007. **36**(6): p. 1106-1118.
6. Rodriguez, C.G., et al., *Experimental investigation of added mass effects on a Francis turbine runner in still water.* Journal of Fluids and Structures, 2006. **22**(5): p. 699-712.
7. Rodriguez, C.G., et al., *Capability of structural–acoustical FSI numerical model to predict natural frequencies of submerged structures with nearby rigid surfaces.* Computers & Fluids, 2012. **64**(Supplement C): p. 117-126.
8. David, V., et al., *Influence of the boundary conditions on the natural frequencies of a Francis turbine.* IOP Conference Series: Earth and Environmental Science, 2016. **49**(7): p. 072004.
9. Avellan, F., et al., *Dynamic Pressure Measurements on a Model Turbine Runner and their Use in Preventing Runner Fatigue Failure*. 2000.
10. Hübner, B., U. Seidel, and S. Roth, *Application of Fluid-Structure Coupling to Predict the Dynamic Behavior of Turbine Components*. Vol. 12. 2010. 012009.
11. Østby, P., et al., *Dynamic Stresses In High Head Francis Turbines*. 2016.
12. Gauthier, J.P., et al., *A numerical method for the determination of flow-induced damping in hydroelectric turbines.* Journal of Fluids and Structures, 2017. **69**(Supplement C): p. 341-354.
13. Chitrakar, S., et al., *Numerical and experimental study of the leakage flow in guide vanes with different hydrofoils.* Journal of Computational Design and Engineering, 2017. **4**(3): p. 218-230.
14. Chitrakar, S., et al., *Numerical investigation of the flow phenomena around a low specific speed Francis turbine's guide vane cascade*. 2016.
15. Eltvik, M., *Sediment erosion in Francis turbines*, in *Department of Energy and Process Technology*. 2013, Norwegian University of Science and Technology.

16. Mack, R., P. Drtina, and E. Lang, *Numerical prediction of erosion on guide vanes and in labyrinth seals in hydraulic turbines.* Wear, 1999. **233-235**(Supplement C): p. 685-691.

17. Moxnes, O.P.D., *Added mass forskyvning av egenfrekvenser*, in *Department of Mathematical Sciences and Technology*. 2011, Norwegian University of Life Sciences.

18. Tipler, P.A. and G. Mosca, *Physics for Scientists and Engineers*. Sixth edition ed. 2008, New York: W.H. Freeman and Company. 1412.

19. Finnemore, E.J. and J.B. Franzini, *Fluid Mechanics with Engineering Applications*. Tenth edition ed. 2002, New York: McGraw-Hill.

20. *Mini Physics - Natural Frequency*. Available from: https://www.miniphysics.com/natural-frequency.html

21. Gulliver, J.S., Arndt, Roger E.A., *Hydropower Engineering Handbook*. 1991, USA: McGraw-Hill Inc.

22. Vinogg, L., Elstad, I., *Hydropower Development: Mechanical Equipment*. Vol. 12. 2003, Trondheim, Norway: Norwegian University of Science and Technology.

23. Hjorthol, L.M. *Preventing hydropower turbine failure*. 2015 20.09.2017]; Available from: https://geminiresearchnews.com/2015/05/preventing-hydropower-turbine-failure/.

24. Thapa, B., O. Dahlhaug, and B. Thapa, *Flow field measurement in guide vane cascade of a high head Francis turbine*. 2016.

25. Brekke, H., *Design and operation of the Kvaerner high head Francis turbines.* 1983.

26. Antonsen, Ø., *Unsteady flow in wicket gate and runner with focus on static and dynamic load on runner*, in *The Department of Energy and Process Engineering*. 2007, Norwegian University of Science and Technology: Trondheim.

27. Hovland, J.M., *Pressure pulsations and stress in a high head Francis model turbine*, in *Department of Energy and Process Engineering*. 2013, Norwegian University of Science and Technology: Trondheim.

28. Rainpower. *Sønnå Høy - Løpehjulshavari*. in *Produksjonsteknisk Konferanse*. 2009.

29. Zobeiri, A., *Investigations of Time Dependent Flow Phenomena in a Turbine and a Pump-Turbine of Francis Type: Rotor-Stator Interactions and Precessing Vortex Rope*, in *FACULTÉ SCIENCES ET TECHNIQUES DE L'INGÉNIEUR*. 2009, Ecole Polytechnique Federale de Lausanne: Lausanne.

30. Qian, R., *Flow Field Measurements in a Stator of a Hydraulic Turbine*, in *Faculté des Sciences et de Génie*. 2008, Université Laval: Quebec.

31. Ruchonnet, N., C. Nicolet, and F. Avellan, *One-dimensional Modeling of Rotor Stator Interaction in Francis pump-turbine.* Proceedings of the 23rd IAHR Symposium on Hydraulic Machinery and Systems, 2006.

32. Van Dyke, M., *An Album of Fluid Motion*. 1982, Stanford, California: The Parabolic Press.

33. Billah, K.Y. and R.H. Scanlan, *Resonance, Tacoma Narrows bridge failure, and undergraduate physics textbooks.* American Journal of Physics, 1991. **59**(2): p. 118-124.

34. *Airplane Life Cycle - Accident Overview*. 20.11.2017]; Available from: http://lessonslearned.faa.gov/ll_main.cfm?TabID=2&LLID=7&LLTypeID=2.

35. Nicolet, C., et al., *On the upper part load vortex rope in Francis turbine: Experimental investigation.* IOP Conference Series: Earth and Environmental Science, 2010. **12**(1): p. 012053.

36. Hou, G., J. Wang, and A. Layton, *Numerical Methods for Fluid-Structure Interaction — A Review*. Vol. 12. 2012.

37. Valkvæ, I., *Dynamic loads on Francis turbines*, in *Department of Energy and Process Engineering*. 2016, Norwegian University of Science and Technology: Trondheim.

38. Qi, H.J. *Finite Element Analysis - Introduction. Lecture notes*. 2006; Available from: https://www.colorado.edu/MCEN/MCEN4173/chap_01.pdf.

39. *ANSYS user manual*. ANSYS.

40. *ANSYS ACT Acoustics manual*. ANSYS.

41. Gjøsæter, K., *Hydraulic Design of Francis Turbine Exposed to Sediment Erosion*, in *Department of Energy and Process Engineering*. 2011, Norwegian University of Science and Technology: Trondheim.

42. Egusquiza, E., et al., *Fluid Added Mass Effect in the Modal Response of a Pump-Turbine Impeller*. Vol. 1. 2009.

43. *ANSYS ACTx R170 - Introduction to Acoustics.* 2017, ANSYS Inc.

44. Zhu, W.R., et al., *Study on stress characteristics of Francis hydraulic turbine runner based on two-way FSI.* IOP Conference Series: Earth and Environmental Science, 2012. **15**(5): p. 052016.

45. Vu, V.H., et al., *EFFECT OF ADDED MASS ON SUBMERGED VIBRATED PLATES*. 2007.

Norges miljø- og biovitenskapelige universitet
Noregs miljø- og biovitskapelege universitet
Norwegian University of Life Sciences

Postboks 5003
NO-1432 Ås
Norway